Existence and Analysis of a Rotating Stall Inception Continuum
&
Development of Concept Questions in Fluid Dynamics

by

Maranda F. Cherry

B.A.Sc. Engineering Physics, Queen's University, 2022

Submitted to the Department of Aeronautics and Astronautics
in partial fulfillment of the requirements for the degree of

MASTERS OF AERONAUTICS AND ASTRONAUTICS

at the

MASSACHUSETTS INSTITUTE OF TECHNOLOGY

September 2024

Authored by:	Maranda F. Cherry Department of Aeronautics and Astronautics August 16, 2024
Certified by:	Edward M. Greitzer H. N. Slater Professor of Aeronautics and Astronautics, Thesis Supervisor
Accepted by:	Jonathan P. How R. C. Maclaurin Professor of Aeronautics and Astronautics Chair, Graudate Program Committee

Existence and Analysis of a Rotating Stall Inception Continuum
&
Development of Concept Questions in Fluid Dynamics

by

Maranda F. Cherry

Submitted to the Department of Aeronautics and Astronautics
on August 16, 2024 in partial fulfillment of the requirements for the degree of

MASTERS OF AERONAUTICS AND ASTRONAUTICS

ABSTRACT

This thesis presents two projects, an analysis of rotating stall inception for axial compressors in turbomachinery, and a description of the creation of Concept Questions for a text on internal flows.

The first part of this thesis identifies flow behavior that defines two routes to rotating stall, known as modal and spike type rotating stall inception. It continues previous studies by MIT and the University of Cambridge surrounding unification of these two stall types under a dynamical system framework. Calculations were carried out for an isolated rotor, with a high hub to tip radius ratio, using TBLOCK, a Reynolds Averaged Navier Stokes solver.

The results show (i) the dependence of stall inception on the compressor axisymmetric pressure rise characteristic and the characterization of mode and spike stall inception as two paths, located at the ends of a continuum of possible paths to stall. (ii) the effect of blade passage accelerations and asymmetry in the onset process, and (iii) the divergence of stall inception from two-dimensionality as a function of the slope of the total-to-static compressor pressure rise characteristic. The calculations show that compressor pressure rise characteristic slopes, $d\psi/d\phi$, less than 0.3 have a stall cell growth rate, σ, that agrees with two-dimensional theory. The divergence of stall inception from two-dimensionality is suggested as a distinguishing feature of spike type stall inception compared to modal type stall inception.

The second part of this thesis encompasses the creation, editing and compilation of Concept Questions for seven book chapters in a new text that describes the use of Concept Questions in teaching (and learning) fluid mechanics. The composition and qualities of a good concept question are defined, and the process of generating and editing questions for the intended audience is discussed.

Thesis supervisor: Edward M. Greitzer
Title: H. N. Slater Professor of Aeronautics and Astronautics

Acknowledgments

I would not have been able to complete this work without the support and advice of many people. I want to thank my thesis supervisor Dr. Ed Greitzer for his steadfast support, his knowledge and his expertise (and for meeting way too often...for way too long). I have learned many things being in the Gas Turbine Lab and I will carry them with me throughout my career.

I want to thank the team that has collaborated and worked many hours on this project: the folks at the University of Cambridge in the Whittle Lab, Dr. Graham Pullan and Dr. Sam Grimshaw, and those at the Gas Turbine Lab here at MIT, Dr. Marshall Galbraith and Dr. Zoltan Spakovszky. Of course I must thank a major collaborator, Marcos Logrono, who stuck it out with me on this project and whose work was critical to my own.

To my friends I have made here at MIT: Lanie, Kinjal, Shaan, Kaila, Alisa, Matthew and so many others, I want to thank you for your support. I want to acknowledge the Indigenous community at MIT, who has given me community and a home away from home.

Lastly, I want to thank my family, my mother Fiona, my two sisters Payton and Taylor, and my father John, who I love dearly and without whom I would not be here. I want to thank my best friends, Chris, Davis, Hattie, and Grace, who have supported me on my journey.

Maarsii, ni kishchiii itaytamikhk. Thank you, I am grateful.

Contents

List of Figures

Nomenclature

Roman

A	area
c	cord length
h	enthalpy
i	$i = \sqrt{-1}$
L	pressure loss
n	harmonic number
p, P	pressure
R	blade radius
s	entropy
t	time
T	temperature
v	absolute velocity
U	blade speed
w	relative velocity
x	cartesian coordinate
y	cartesian coordinate

Greek

α	absolute angle
β	relative angle

γ	stagger angle
θ	circumferential angle, location
λ	blade passage inertia
μ	stator and rotor blade passage inertia
ρ	density
σ	perturbation growth rate ($\frac{\Delta p/\rho U_t^2}{\tau}$), first harmonic growth rate
σ_n	real system eigenvalues
τ	non-dimensional time ($\tau = tU/R$)
ϕ	flow coefficient (V_x/U)
ψ	pressure rise ($\Delta P/\rho U^2$)
ω	perturbation rotation rate
ω_n	imaginary system eigenvalues
Ω	rotor frequency
ζ	loss coefficient

Prefixes

δ	perturbation (small amplitude)
Δ	difference

Superscripts and Subscripts

TT	total-to-total
TS	total-to-static
I	isentropic
$\bar{}$	mean value
t	stagnation, tip
r	radial
R	rotor
S	stator
∞	ambient, far upstream condition

Part I

Rotating Stall Inception

Chapter 1

Introduction

Compressor instability is an important concern in turbomachinery design because useful operation of compressors can be limited by flow instabilities. Rotating stall and surge are two such types. During surge, a compressor experiences flow reversal as the mean flow moves back and forth between stalled and unstalled operation. During rotating stall, one, or multiple, regions of stalled flow rotate around the annulus of a blade row, typically between 20% to 50% that of the rotor rotation rate [1]. This stalled region, referred to as a stall cell, propagates in the direction of rotation of the rotor [2]. Rotating stall causes large stresses on blading, and for an aircraft engine, a substantial reduction in thrust [3].

Rotating stall inception is associated with the growth of small-amplitude flow field disturbances that are intrinsically nonaxisymmetric [4]. The current view is that there are two routes to stall, noted as modal and spike stall inception [5], which have been considered to be distinct phenomena [6]. Modal stall inception consists of the growth of long length scale perturbations, on the order of the compressor circumference. Spike-type stall inception is characterized by short-length scale disturbances, on the order of a blade passage, that appear as spike-like waveforms in velocity and pressure measurements taken around a rotor blade [2]. The present research aims to understand the mechanisms associated with both types of behavior.

1.1 Thesis Scope

This thesis identifies flow behavior that defines modal and spike type stall inception in a unified manner. It continues previous work, by a MIT-Cambridge team, to capture the two stall inception types under a single dynamical framework. The effect of the gradient of the axisymmetric compressor pressure rise characteristic, $d\psi/d\phi$, with respect to stage flow coefficient ϕ, on the path to stall and its divergence from two-dimensionality is assessed. The influence of two parameters, blade passage inertia and blade restagger, on stall inception is also discussed.

1.2 Contributions

The main contribution of this thesis is the suggestion of an updated definition of modal and spike stall inception, and further unification of these two paths to stall, as previously theorized by the Gas Turbine Lab at MIT and the Whittle Lab at the University of Cambridge. Consistent with the Cambridge work, modal and spike type stall inception are classified as parts of a continuum of stall inception types, and the nature of the continuum including the existence of intermediate stall types is described. The role of the slope of the compressor pressure rise characteristic, $d\psi/d\phi$, is seen to be key in prediction of stall types. The growth rate of stall cells during inception is shown to be consistent with two-dimensional linear theory and the divergence of stall inception from two-dimensionality is suggested as a distinguishing feature of spike type stall inception compared to the two-dimensional, modal type, stall inception.

Chapter 2

Background

2.1 Rotating Stall

Rotating stall occurs when fluid passing through a compressor blade row with high loading experiences localized nonuniformity, causing flow separation. The separated flow region results in increased incidence on one side of the stalled region, and decreased incidence on the other side due to diversion of streamlines from the blockage. The section of decreased incidence causes the stalled flow to unstall, so the stalled region propagates around the blade row of the compressor [2]. The stalled region rotates in the same direction as the rotor and at a rate less than that of the blade speed in the absolute reference frame, typically around 20% to 50% [5]. A depiction of the onset of stall is provided in Figure 2.1, [3]. The flow diverts from the stalled blade, B, and reducing the incidence on blade C, causing propagation from right to left, and stalling blade A.

Rotating stall can be exhibited as single or multiple stall cells, and each cell can range from spanning a few blade widths to more than half the blade row annulus. Moreover, the cell can span from the blade hub to tip, *full-span stall*, which results in the cell extending axially throughout a compressor, or it can encompass a localized region of the blade, near the hub, or near the tip, as *part-span stall*, resulting in a stalled region in part of the compressor

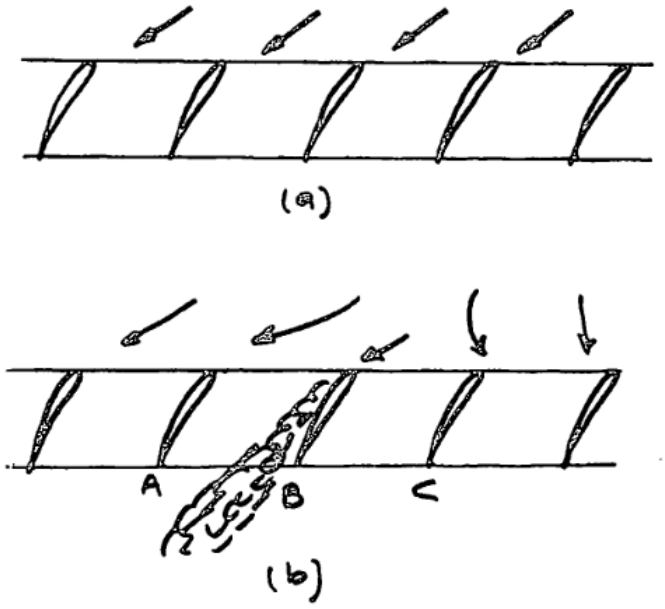

Figure 2.1: Onset of rotating stall due to flow separation [3].

or one blade row [1], [3] . There are two currently identified routes to rotating stall, modal, and spike stall, with differentiating features. The two routes, which have been considered to be distinct, are described in the next two sections [2], [5].

2.1.1 Definitions

For the thesis, a number of terms, the first three of which are displayed in Figure 2.2, need to be defined:

- The *rotating stall inception regime* is the time within which the magnitude of fluid perturbations are growing from 10^{-3} to 10^{-2} the mean flow values. Perturbations are considered small in this regime.

- The *first observation point* for rotating stall is the point at which flow instabilities reach a magnitude of 10^{-3} that of the mean flow value.

- Disturbances associated with rotating stall will be considered *large amplitude* once they have grown past a magnitude of 10^{-2} that of the mean flow value. Development past

this magnitude will not be considered in this thesis.

- A stall *cell* is defined as a region of flow within which the flow has stalled or is stalling. In this work, the stall cell is considered a region of flow with growing perturbations.

- The stall inception *route*, or *path* is the behavior of the flow observed prior to development of large amplitude perturbations. Modal inception and spike type stall inception are two types of this.

- The growth rate, σ, of the perturbations is the non-dimensional rate of increase in magnitude. σ_n is the non-dimensional growth rate of the nth harmonic of flow disturbances (and the real part of the eigenvalues of the isolated rotor system).

- The rotation rate, ω, of the perturbations is the non-dimensional rate at which the the forming stall cell rotates around the rotor. ω_n is the non-dimensional growth rate of the nth harmonic for flow disturbances (and the imaginary part of the eigenvalues of the isolated rotor system).

- ψ^{TS} denotes the axisymmetric, compressor total-to-static pressure rise characteristic $(P_2 - P_{t_1}/\rho U^2)$.

- The *characteristic slope*, $d\psi/d\phi$, is the gradient of the compressor pressure rise characteristic, with respect to flow coefficient, ϕ[1].

The top plot in Figure 2.2 shows the pressure traces at 11 circumferential points as a function of time. The flow perturbations can be expressed as a Fourier series containing the amplitude and position of the perturbation waveform. The magnitudes of the pressure perturbations are shown in the bottom figure using a spatial Fourier decomposition for the first six harmonics. The harmonics can be considered independent from each other for small perturbations, which occur within the *rotating stall inception regime* identified above [4]. A

[1]For further information see the list of symbols given in the Nomenclature section

perturbation can be represented as: $\delta\phi \approx REAL(Ce^{in\theta})$, where C is a coefficient describing the amplitude of the disturbance [4].

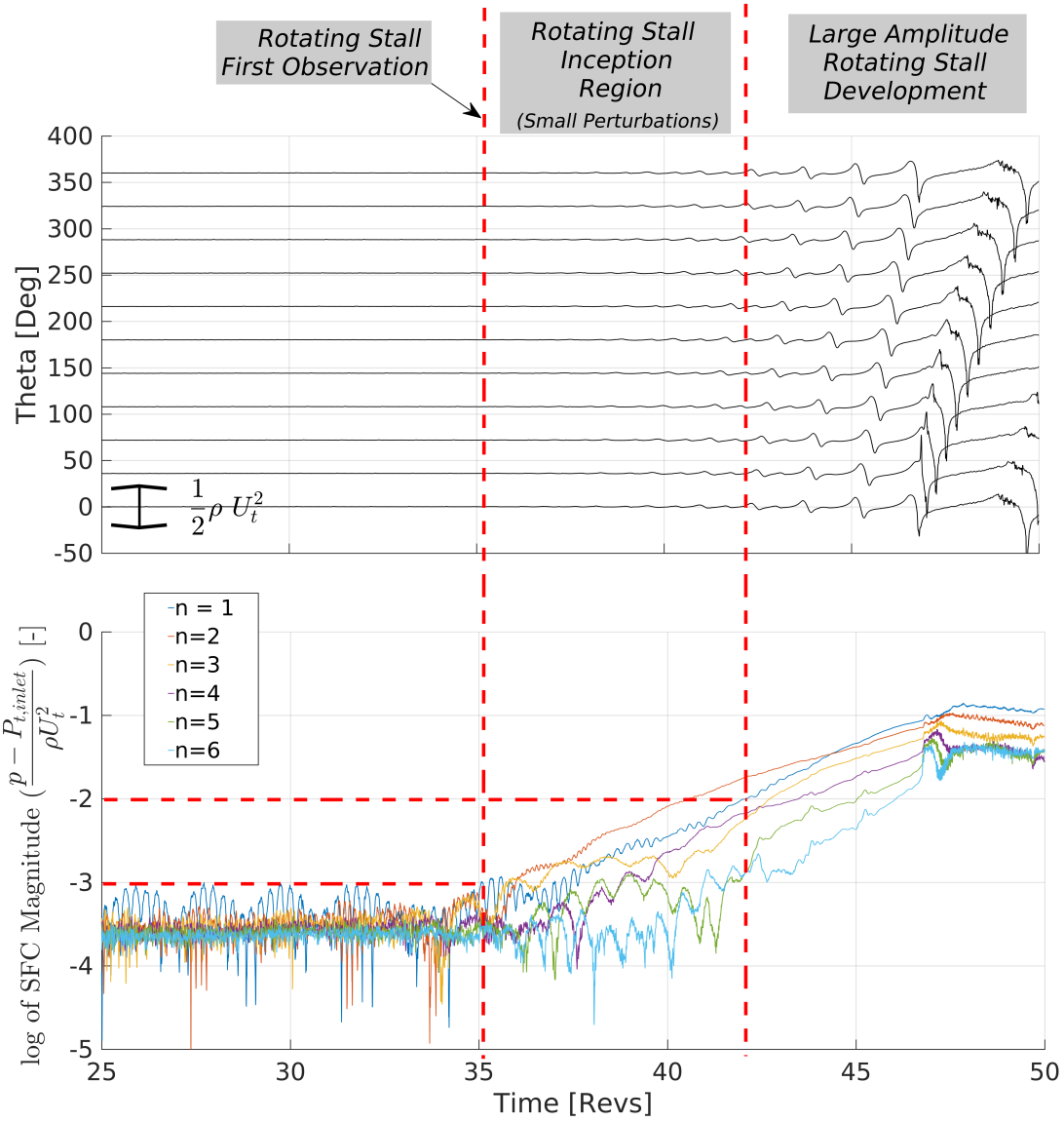

Figure 2.2: Definition of stall terms as defined in the context of TBLOCK simulations. The top plot shows the pressure traces in time at 11 circumferential points along the annulus, the bottom plot gives the magnitude of the spatial Fourier harmonics for the mean pressure perturbations in time.

2.1.2 Modal Stall Inception

Modal stall is associated with the growth of small amplitude, long wavelength (on the scale of the annulus circumference, much larger than that of the blade passage), sinusoidal oscillations in pressure and velocity that develop over tens of rotor revolutions [2],[6]. In the inception regime the growth rate of the perturbations is exponential. Figure 2.3 shows an example of modal type stall inception from hot wire measurements taken of velocity traces at six different circumferential points around the blade row in time [5]. There is a smooth growth of perturbations, propagating around the rotor blade, and growing into a fully developed stall cell.

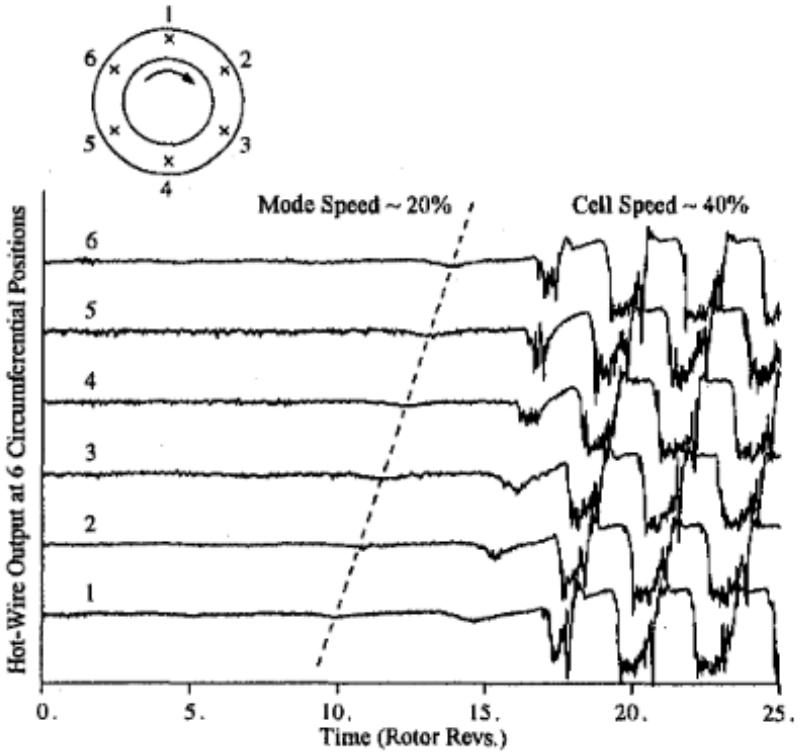

Figure 2.3: Example of modal stall inception from experimental hot-wire measurements by Camp and Day [5]. The velocity traces in time are given at six circumferential positions.

2.1.3 Spike Stall Inception

Spike stall is defined by a sudden growth of the perturbations, which is seen as a "spike" in the evolution of pressure and velocity perturbations at the rotor face. The initial cell is localized to a narrow region of the annulus (several blade pitches) and rotates faster than modal perturbations, around 60% to 80% [2]. The time from inception to fully developed stall is on the order of one to several rotor revolutions [4]. The circumferential length scale is one to several blade pitches [6].

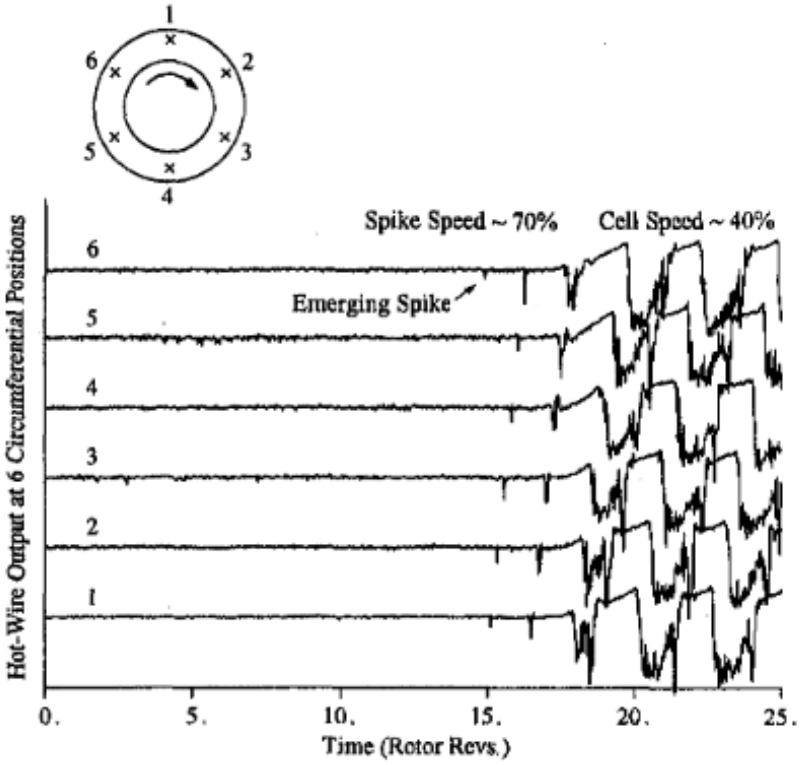

Figure 2.4: Example of spike stall inception from experimental hotwire measurements by Camp and Day [5].

2.1.4 Compressor Pressure Rise Characteristic

The compressor pressure rise characteristic used here is the total-to-static axisymmetric pressure rise, $\psi^{TS} = \frac{P_2 - P_{t_1}}{\rho U^2}$, as a function of flow coefficient ($\phi = V_x/U$), the axial velocity

divided by the blade speed of the rotor. The axisymmetric total-to-static characteristic varies locally with blade radius and is assumed to be a smooth curve [7]. Flow in the negatively sloped characteristic regime is dynamically stable in that growth of flow perturbations are damped. The positively sloped regime has the opposite effect in that perturbations in the flow grow in time [4].

A canonical example of a smooth, S shaped, curve that has been used to represent the axisymmetric total-to-static pressure rise characteristic is a cubic curve [7].

$$\psi_c^{TS}(\phi) = \psi_{c_0} + H(1 + \frac{3}{2}(\frac{\phi}{W} - 1) - \frac{1}{2}(\frac{\phi}{W} - 1)^3), \tag{2.1}$$

where ψ_{c_0} is the axisymmetric shut-off value, and W and H are coefficients that describe the values of $\psi_{peak} = 2H + \psi_{c_0}$ and $\phi_{peak} = 2W$ for the characteristic. Figure 2.5 shows the general curve shape.

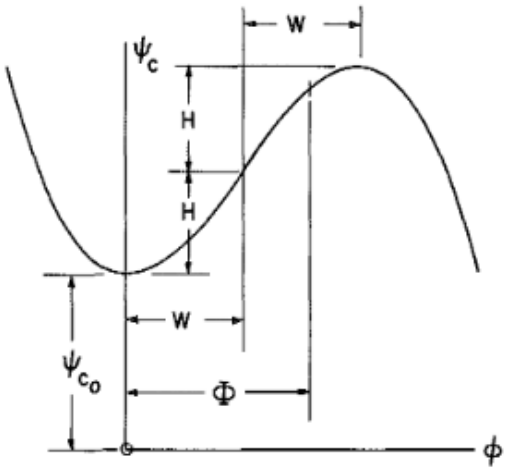

Figure 2.5: Diagram showing the notation used to define the cubic axisymmetric characteristic [7].

2.1.5 Additional flow parameters

Three parameters described below pertain to this thesis through their effect on the compressor pressure rise and flow instability.

Blade Restagger

For this work, blade restagger is defined as a variation in the inlet relative flow angle β_1. Small changes in the blade inlet relative angle affect the local pressure rise across the blade. This effectively changes the slope of the local characteristic, causing asymmetry in the flow. At the peak of the compressor pressure rise, part of the circumference of the compressor is on the unstable side of the characteristic, amplifying the flow disturbances. Blade restagger is used in this thesis to introduce asymmetric perturbations to the flow, as was used by Logrono in [8], and by Pullan and Grimshaw in [9]. This definition of blade restagger differs from the conventional definition, where the stagger angle of a blade is changed (restaggered), affecting both inlet and exit flow angles [5].

Blade Passage Inertia

Unsteady blade passage fluid acceleration, also called blade row inertia, is defined in Equation 2.2 for a rotor.

$$\lambda = \sum_{rotors} \frac{c_x}{R \cos^2 \gamma}, \tag{2.2}$$

where R is the mean radius, c_x is the axial chord length, and γ is the blade stagger angle. The effective path length fluid travels is longer than the axial length as it passes between rotor blade passages, and part of the compressor pressure rise is devoted to accelerating flow in the blade passages [7], [10]. This requires a nonsteady pressure differential across the blade row. Non-dimensional values used in the present calculations were between $\lambda = 0.1 - 0.2$, based on the range for typical civil engines [4].

Loss Lag

The pressure loss through a blade row in unsteady flow will depart from quasi-steady behavior due to viscous effects [7]. This *loss lag*, models the unsteady viscous response of a blade row [4]. The time lag constant, τ, depends on the response time of the boundary layers of the

blades. Loss lag has a stabilizing effect on the flow [4]. Loss lag will not be considered within this thesis.

2.2 Two Dimensional Linearized Theory for Rotating Stall

Two-dimensional flow field models have been developed to analyze rotating stall onset in high hub-to-tip radius ratio (HTR) compressors. The compression system considered consists of an inlet and exit duct and a compressor; the small-amplitude perturbations do not affect the mean pressure rise or mass flow within the compressor and the inclusion of plenum and throttle dynamics is not necessary [4]. The compressor is modeled using the steady axisymmetric compressor pressure rise characteristic, ψ^{TS}, with additional terms to include the effects of asymmetry and unsteady flow.

For perturbations that are small compared to the mean values, the effect on pressure and velocity of the flow throughout the rotor can be described via a linear analysis. In addition, this allows adoption of a simplified (and well known) approach to stall inception called an actuator disk analysis. The actuator disk method used within this thesis and simulations is described in [8].

For the approximation of no loss lag, it is known that perturbations begin to grow, and flow becomes unstable, when

$$\frac{\partial \psi^{TS}}{\partial \phi} > 0 \quad [4]. \tag{2.3}$$

This is an important conclusion indicative of the point where rotating stall occurs within a compressor [1], [5].

2.2.1 The Stenning Model

For a compressor blade row with a high hub to tip radius ratio, the flow is assumed to be two dimensional. Viewing the flow from a rotating reference frame attached to the blade, the static pressure rise across the row is defined as

$$C_p = \frac{\Delta P}{\frac{1}{2}\rho w_1^2} \tag{2.4}$$

where w is the inlet velocity of the flow in a reference frame attached to the rotor blade. Stenning uses this parameter, linearizes the equations of conservation of mass and momentum across a blade row, and solves the system of differential equations for the eigenvalues, thus finding an expression for the growth rate and rotation rate of a stall cell during stall inception [3]. These expressions, which can be transformed to be in the absolute reference frame, are in terms of the rotor total-to-static characteristic. (The present treatment includes the effects of the downstream pressure perturbations which decreases the predicted rotation rate ω_n by $\frac{1}{2}$ compared to Stenning's results.)

$$\sigma_n = \frac{n}{2}\frac{\partial \psi^{TS}}{\partial \phi} \text{ and } \omega_n = \frac{n}{2}(2\psi^{TS} - \phi\frac{\partial \psi^{TS}}{\partial \phi}) + 1 \tag{2.5}$$

where n is the number of the harmonic, σ_n is the growth rate of the harmonic, and ω_n is the rotation rate. These are derived by Logrono in [8]. The focus of this thesis is on the growth rate of flow disturbances during inception. Current work is being done to compare the rotation rate of the stall cell predicted by the linear theory with TBLOCK simulations, but this is outside of the scope of the thesis.

2.2.2 The Spakovszky Model

Spakovszky used a modular approach to modeling a compression system. The equations describing each component, such as an axial duct, rotor, or stator, are represented as a transmission matrix that can be linked to other components [10]. Three expressions define the flow across the rotor actuator disk: Continuity, conservation of axial momentum, and pressure rise across the actuator disk. Logrono [8] describes the Spakovszky expressions for the isolated rotor case. Assuming there is no inlet swirl, and neglecting loss lag, the expression for the real part of the eigenvalues of the system (growth rate of the harmonics

of the stall cell) is

$$\sigma_n = \frac{tan\beta_2 + \frac{\partial L_R^{SS}}{\partial tan\beta_1}\frac{tan\beta_1}{\phi} - \phi(1 + tan^2\alpha_2) + tan\alpha_2}{\lambda_{rotor} + \frac{2}{n}} \tag{2.6}$$

where α_2 is the absolute exit angle of the flow and β_1 is the inlet flow angle in the rotor reference frame. If, for the mean flow, it is assumed that $\phi = -\frac{1}{tan\beta_1}$, the expression for the imaginary part of the eigenvalues of the system (rotation rate of the harmonics of the stall cell) is

$$\omega_n = \frac{\left[\left(\frac{\partial L_R^{SS}}{\partial tan\beta_1} - \frac{\partial \psi_I^{TT}}{\partial tan\beta_1}\right)\frac{1}{\phi} + n\lambda_{rotor} + 1\right]}{\lambda_{rotor} + \frac{2}{n}}. \tag{2.7}$$

Equation 2.7 is the updated expression produced by Grimshaw, Pullan, Logrono and Cherry for the rotation rate as of December 2023 but the updated derivation is outside of the scope of this work. For consistent assumptions (inclusion of downstream pressure perturbations, neglecting loss lag, neglecting blade passage inertia) the Spakovszky expressions for growth and rotation rate and those of Stenning are equivalent. Logrono [8] show this for the growth rate.

Equation 2.8 gives the growth rate of perturbations from the linear analysis during stall inception, in terms of the total-to-static pressure rise characteristic. This analytical expression, for the n=1 harmonic, will be used to compare against results from TBLOCK simulations in Section 4.4.

$$\sigma_n = \frac{\frac{\partial \psi^{TS}}{\partial \phi}}{\lambda_{rotor} + \frac{2}{n}} \tag{2.8}$$

2.3 Assumptions

It is useful to list the following assumptions that are made in this thesis:

- The effects of viscosity and heat transfer are neglected

- The flow upstream of the blade row is irrotational
- The effects of time delay due to blade passage losses τ are neglected
- The analysis is carried out for an isolated rotor blade row
- The blade row is modeled as an actuator disk with unsteady blade passage accelerations (inertia) and asymmetric blade restagger
- The Mach number is low enough such that compressibility effects can be neglected
- The effects of deviation from the rotor exit are neglected and the blade exit angle is assumed to be constant

Chapter 3

Computational Setup

In this chapter, the actuator disk analysis is briefly introduced and the computation procedure used in the thesis, TBLOCK, is described for rotating stall inception in an isolated axial compressor rotor. The geometry used for the isolated rotor is not limited to two dimensions and allows three-dimensional flow. The simulation set up, and computational procedure, is discussed.

3.1 Actuator Disk Method

The actuator disk analysis was implemented within a stall dynamics model developed by Cambridge University[1] [6]. The actuator disk, Figure 3.1, simulates flow across a blade row; the disk is a discontinuity within the flow, with the performance of the blade rows described by loss and pressure rise characteristics. The change in pressure and flow angle are based on matching conditions across the disk (set by initial parameters and the pressure rise and angle characteristic). The method is described in depth by Logrono [8]. The operating point of the flow is changed by throttling the flow using a nozzle. For compressible flow, Hynes and Joo [11] suggest five matching conditions across the actuator disk that are applied to each radial location at the disk. This includes conservation of mass, conservation of rothalpy

[1] G. Pullan at the Whittle Lab

and conservation of radial momentum. The relative exit flow angle β_2, and the entropy rise, through a loss coefficient $\zeta = \frac{T\Delta s}{\frac{1}{2}w_1^2}$ across the disk must also be given.

To determine the loss coefficient ζ, the difference between the isentropic and real compressor pressure rise characteristics is calculated. The local total-to-static pressure rise across a blade row is defined as:

$$\frac{p_2 - p_{t1}}{\rho U^2} = \psi^{TS}(\phi) - \lambda\frac{\partial\phi}{\partial\theta} - \mu\frac{\partial\phi}{\partial\tau}, \tag{3.1}$$

where λ is the blade passage fluid inertia for the rotors, μ is the blade passage fluid inertia for rotors and stators (no stators appear in this work), and $\tau = tU/R$ is the non-dimensional time [10], [12]. Station 1 denotes the flow just upstream of the rotor, and Station 2 denotes the flow just downstream of the rotor. The total-to-static characteristic that describes the pressure rise across the compressor is

$$\psi^{TS}(\phi) = \psi_I^{TS}(\phi) - L_R(\phi) - L_S(\phi), \tag{3.2}$$

where L_R and L_S are the total pressure losses for the rotor and stator blade rows [10]. For the case covered in this thesis, the isolated rotor, the loss is dependent on only rotor loss, L_R.

The isentropic compressor characteristic, $\psi_I^{TS}(\phi)$, is derived beginning with Equation 3.3,

$$Tds = dh_t - \frac{1}{\rho}p_t = 0, \tag{3.3}$$

where there is no change in entropy and the enthalpy rise from work done by the compressor is directly equal to the increase in stagnation pressure. The change in enthalpy across a compressor blade row is described by the Euler Turbine equation for no change in radius across the blade row:

$$\Delta h_t = \Omega r \Delta V_\theta. \tag{3.4}$$

Equation 3.4 can be written as

$$\frac{\Delta h_t}{U^2} = \psi^{TT} \Omega r \Delta V_\theta, \tag{3.5}$$

where ψ^{TT} is the total-to-total rotor characteristic. Across an isolated rotor, Equation 3.4 is

$$\psi_I^{TS} = \frac{1}{2}(1 - \phi^2(1 + tan^2\beta_2) - 2tan\alpha_1), \tag{3.6}$$

where β_2 is the rotor blade metal angle, and α_1 is the inlet swirl angle in the absolute reference frame.

The loss coefficient can be written in terms of the compressor pressure rise characteristic:

$$\zeta = \frac{T\Delta s}{\frac{1}{2}w_1^2} = \frac{2}{1+\phi^2}(\psi_I^{TS} - \psi^{TS}). \tag{3.7}$$

Further description of these parameters is given by Logrono [8].

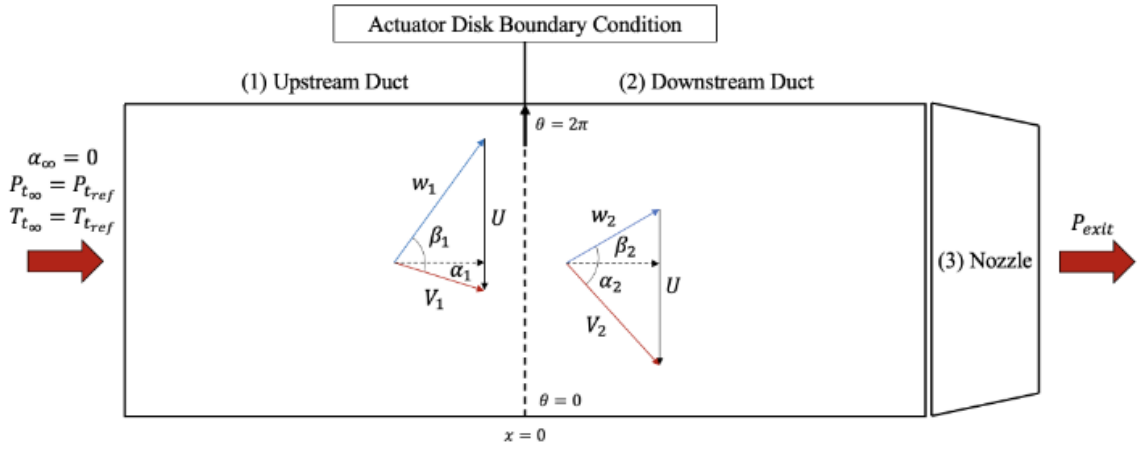

Figure 3.1: TBLOCK actuator disk schematic from Logrono [8].

3.2 Simulation Set Up

3.2.1 TBLOCK

TBLOCK is a multi-grid Reynolds Averaged Navier-Stokes (RANS) solver built with the goal of predicting main blade path and secondary gas path flows in turbomachinery [6]. TBLOCK uses a finite-volume time-marching, second order in space scheme, with three multigrid levels and a single step explicit time integration [6]. The mesh geometry used here consists of a uniform cylindrical annulus. For the high hub-to-tip radius (HTR) ratio, isolated rotor case presented in this thesis, the duct has uniform flow far upstream with a nozzle downstream of the duct as a throttle. The "weak" radial boundary conditions imposed at the hub and tip of the actuator disk annulus, and at the inner and outer diameters of the ducts are such that the mass flux at the boundary is zero [13]. This allows for radial velocity at the hub and tip of the disk to be non-zero and is seen in simulations conducted in TBLOCK for this thesis.

3.2.2 Geometry

The geometry of the isolated rotor in the thesis, Figure 3.2, has also been used by Logrono [8]. The blade geometry is a section of a compressor rig used in experiments by Cambridge. The original geometry has a HTR of 0.75. The geometry in this work was designed to examine a flow geometry that accomplished two things: one was to be nearly two-dimensional to isolate the effects of radial variations in mean flow. To do this, the HTR was increased to 0.9999. It was also desired to keep the ratio of radial dimension (scale) to axial dimension, so there would be the possibility of three dimensional flow, as in the actual geometry. To do this, the geometry used was a circumferential section 0.1440° in extent. The result is nearly a two-dimensional cascade. Periodic boundary conditions are imposed at the edges of the section (from one circumferential end to another). In summary, the radial span and

the circumferential length scales are representative of the physical geometry and allow for three-dimensional flow. An image of the geometry is given by Logrono in [4].

The actuator disk represents the rotor by 101 circumferential and 7 radial points. The 7 radial points provide a cell height about half of a compressor blade pitch. The inlet and exit ducts on both sides of the actuator disk each have their length twice the outer disk circumference. The mesh has 201 axial points that span the geometry from inlet to exit [8].

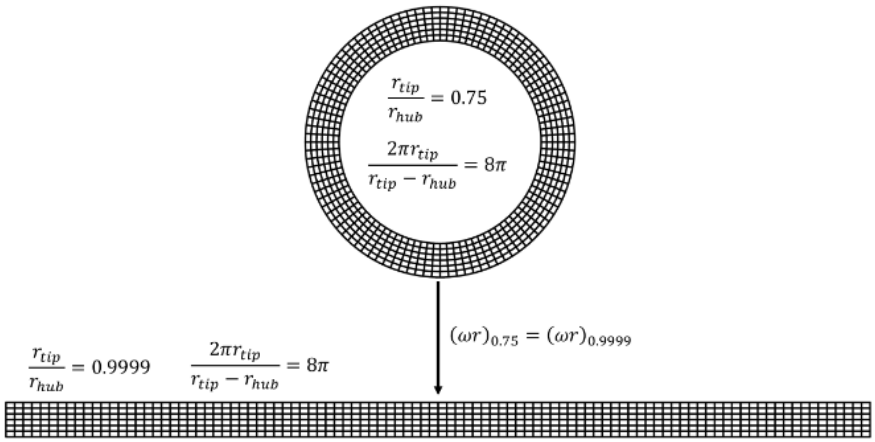

Figure 3.2: TBLOCK actuator disk mesh and geometry for the 0.9999 HTR ratio rotor. The 0.9999 HTR ratio geometry is slightly curved into a wedge shape (not pictured here) [8].

3.2.3 Inputs

Compressor Total-to-Static Characteristic

To analyze the relationship between stall inception type and characteristic, the axisymmetric characteristic used in the simulations, Figure 3.3, was chosen to have a linearly sloped positive gradient, such that the slope can be varied and the effect of this variation isolated. For the negatively sloped part of the characteristic, a variation of the Moore-Greitzer cubic axisymmetric curve, Equation 2.1, was used to set the total-to-static pressure rise characteristic that describes the flow across the actuator disk. The chosen values for the terms in the curve are $\psi_{c_0} = 0, H = 0.1025$, and $W = 0.185$. The middle part of the characteristic

(solid line) is the variable sloped line, and the cubic characteristic is to the right of the peak[2] (dashed line). The leftmost leg of the characteristic (dotted line) is such that the line passes through the origin. Reverse flow does not occur within the *rotating stall inception regime* (defined in Section 2.1.1), so the behavior of the compressor during reverse flow was not specified by this characteristic.

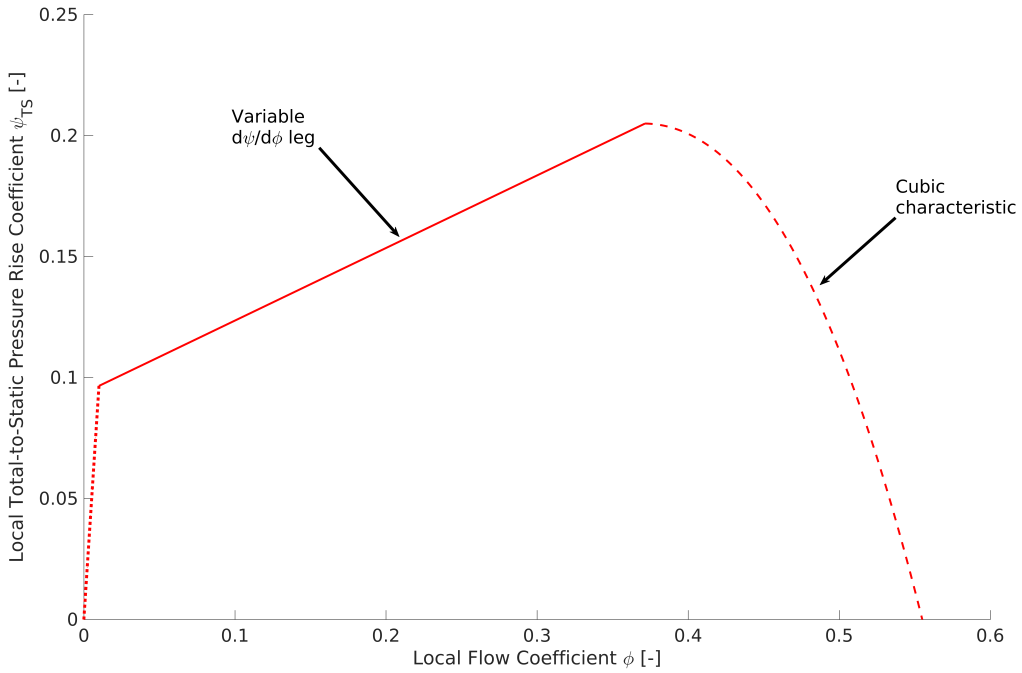

Figure 3.3: Characteristic used for simulations with a variable middle leg to examine the effect of the slope of the characteristic on stall inception.

[2]Logrono used the Moore-Greitzer cubic characteristic to define an operating point for steady state calculations with the same parameters for ψ_{c_0}, H, and W. He then switched to a positively sloped, linear, characteristic to compute the transient behavior.

Parameters

The following parameters applied to the simulations performed:

- For cases with blade restagger[3], a 0.1 RMS *top-hat* blade angle restagger was applied to a 0.007° section of the 0.1440° wide actuator disk. Blade restagger is given in Figure 3.4.
- For cases with blade passage inertia the inertial parameter was set to $\lambda_{rotor} = 0.2$, the nominal value used by Cambridge and Logrono [8].
- The blade exit angle was constant at $\beta_2 = 51.45°$ at all points around the actuator disk.

Section 4.3 in Chapter 4 describes cases run without blade restagger, and without blade passage inertia, respectively.

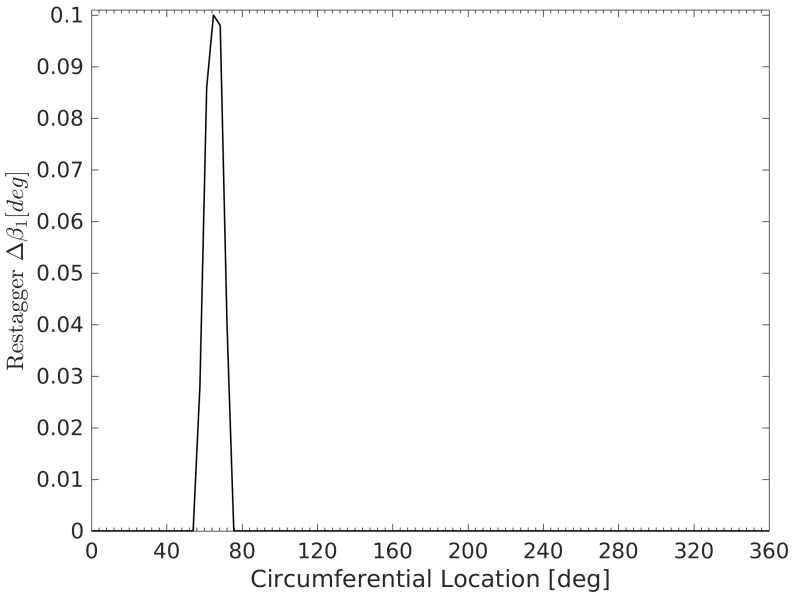

Figure 3.4: Blade restagger $\Delta\beta_1$ applied to the inlet relative flow angle β_1. Note that this restagger is mapped onto the circumferential extent of the geometry $(0.00 - 0.1440°)$.

[3]see definition of restagger in Section 2.1.5

3.2.4 Simulation Procedure

A steady solution for an operating point to the right of the peak of the axisymmetric pressure rise characteristic, Figure 3.3, was first found and used to initialize the unsteady solution. The domain inlet total pressure and temperature were specified as uniform. From the stable operating point, the flow was throttled, using the convergent downstream nozzle, to move the flow to the left along the characteristic to the peak. The ramping scheme for throttle change is linear, with the nozzle back pressure ramped for 5 rotor revolutions and then held for 20 rotor revolutions. (This follows the CFD Hewkin-Smith ramp-and-hold method as a best practice [9]). The ramp-and-hold method was repeated until fluid disturbances were found to grow, and rotating stall inception was observed. This occurred at, or just to the left of, the peak of the pressure rise characteristic. The TBLOCK simulations failed when perturbations became large in amplitude, but this was not an issue for the study of the rotating stall inception regime.

Chapter 4

The Mode-Spike Continuum

In this chapter, the relationship between stall inception behavior and compressor pressure rise characteristic is discussed, based on rotating stall calculations performed with the TBLOCK actuator disk method. The simulations show a continuum of features between modal and spike stall inception, in agreement with other results from the MIT-Cambridge team. The qualities associated with the continuum are described, including the specific effects of asymmetry in blade stagger and blade passage accelerations (inertia), Section 4.3. A comparison is made between the TBLOCK calculations and two-dimensional linear theory. The departure of stall from two dimensional behavior associated with steepening of the compressor pressure rise characteristic is also discussed. The results are used to suggest an updated definition of modal and spike stall inceptions.

4.1 Indication of Continuity Between Modal and Spike Type Stall Inception

As defined in Section 2.1, the two routes to rotating stall inception differ in their growth rate and rotation rate. Modal stall inception has a slower growth, and a slower rotation rate than spike stall inception. Different rotor characteristics were used to investigate the effect of the

compressor pressure rise on stall, (as also done by Pullan and Logrono [8]). The simulation set up was discussed in Chapter 3 using the pressure rise characteristic in Figure 3.3. The slope of the straight line on the positively sloped part of the characteristic is termed the "characteristic slope", or $d\psi/d\phi$, within this thesis. The range of characteristic slopes in the simulations was from $d\psi/d\phi = 0.05$ to 3.0.

Unless otherwise specified, all runs had blade restagger and included blade passage inertia (see Section 3.2.3). The same cubic equation for the characteristic at values of ϕ greater than the peak was used for all cases. The pressure rise, ψ^{TS}, and the flow coefficient, ϕ, at the peak were 0.205 and 0.372 respectively. All cases become unstable at the same throttle coefficient and back pressure, corresponding to the peak of the characteristic ($d\psi/d\phi = 0$).

Evolution of Pressure Perturbations at Stall Inception

Rotating stall inception features will be shown for the six different values of positive slope of the characteristic given in Figure 4.1, ranging from $d\psi/d\phi = 0.1$ to 0.6. Figure 4.2 shows the growth of the pressure perturbations for these cases, from the onset of instability to the development of large amplitude perturbations. The pressure traces are plotted at 11 circumferential points around the annulus[1], with the direction of rotation indicated by a red arrow. The black arrow in the lower left of each plot indicates the dynamic pressure magnitude, based on rotor speed, to provide context for the size of the pressure perturbations. Simulations are ended due to solver failure (discussed in Section 3.2.4) so the pressure traces in Figure 4.2 for the last four simulations are cut off. As mentioned, the cut off occurs outside of the stall inception region and is outside of the thesis scope.

[1]These points correspond to locations in the 0.1440 degree segment

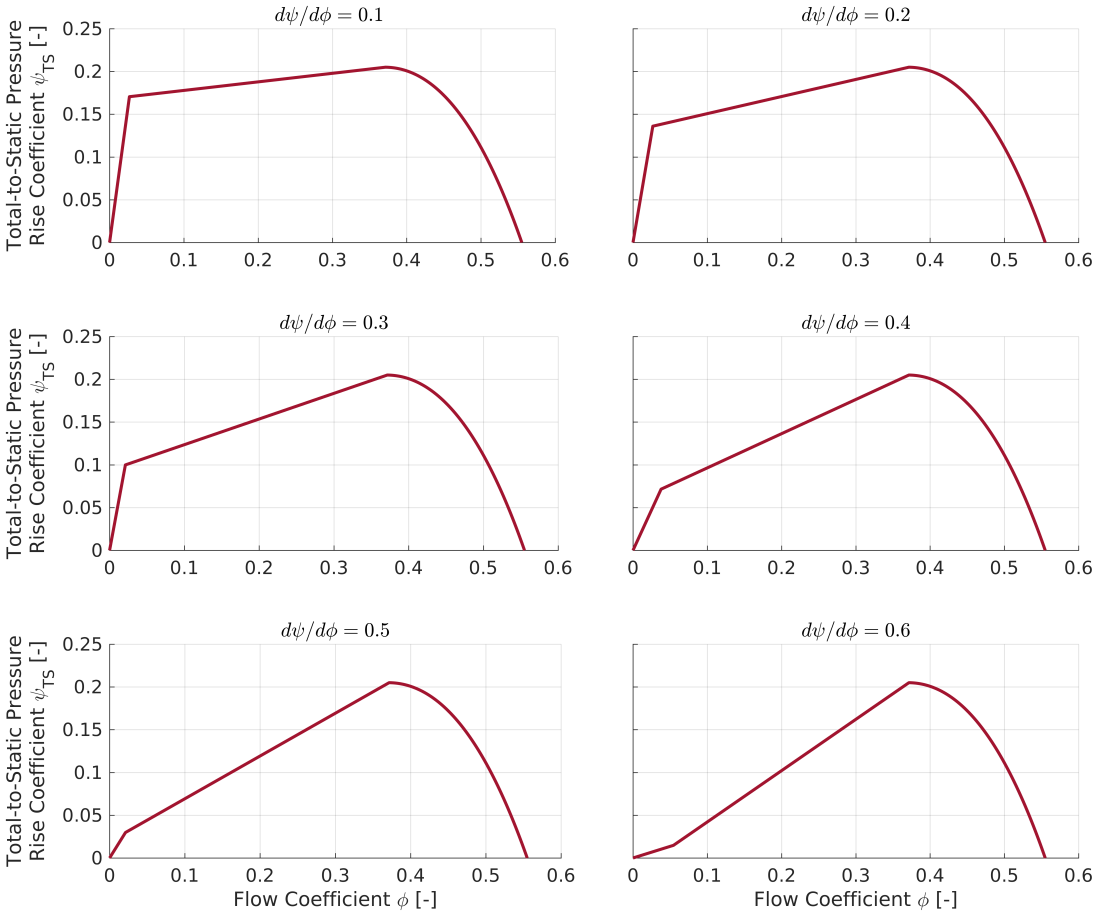

Figure 4.1: Axisymmetric total-to-static compressor pressure rise characteristics ψ^{TS} with slopes $d\psi^{TS}/d\phi$ from 0.1 to 0.6.

The two cases with the shallowest characteristic slope, $d\psi/d\phi = 0.1$ and 0.2, have pressure waves that grow over more than five rotor revolutions. This oscillating, long wavelength, growth is associated with modal stall inception, as discussed in Section 2.1. As the slope is increased, there is a transition into sharper, spike-like waveforms and a shortening of the stall inception region. For the steeper sloped cases, $d\psi/d\phi = 0.5$ and 0.6, the stall inception regime is less than two rotor revolutions, a quality associated with spike-type stall inception, as also in Section 2. The transition between these two behaviors, as the positive slope is increased, indicates intermediate stall inception types: stall inception that has both modal and spike stall inception like qualities.

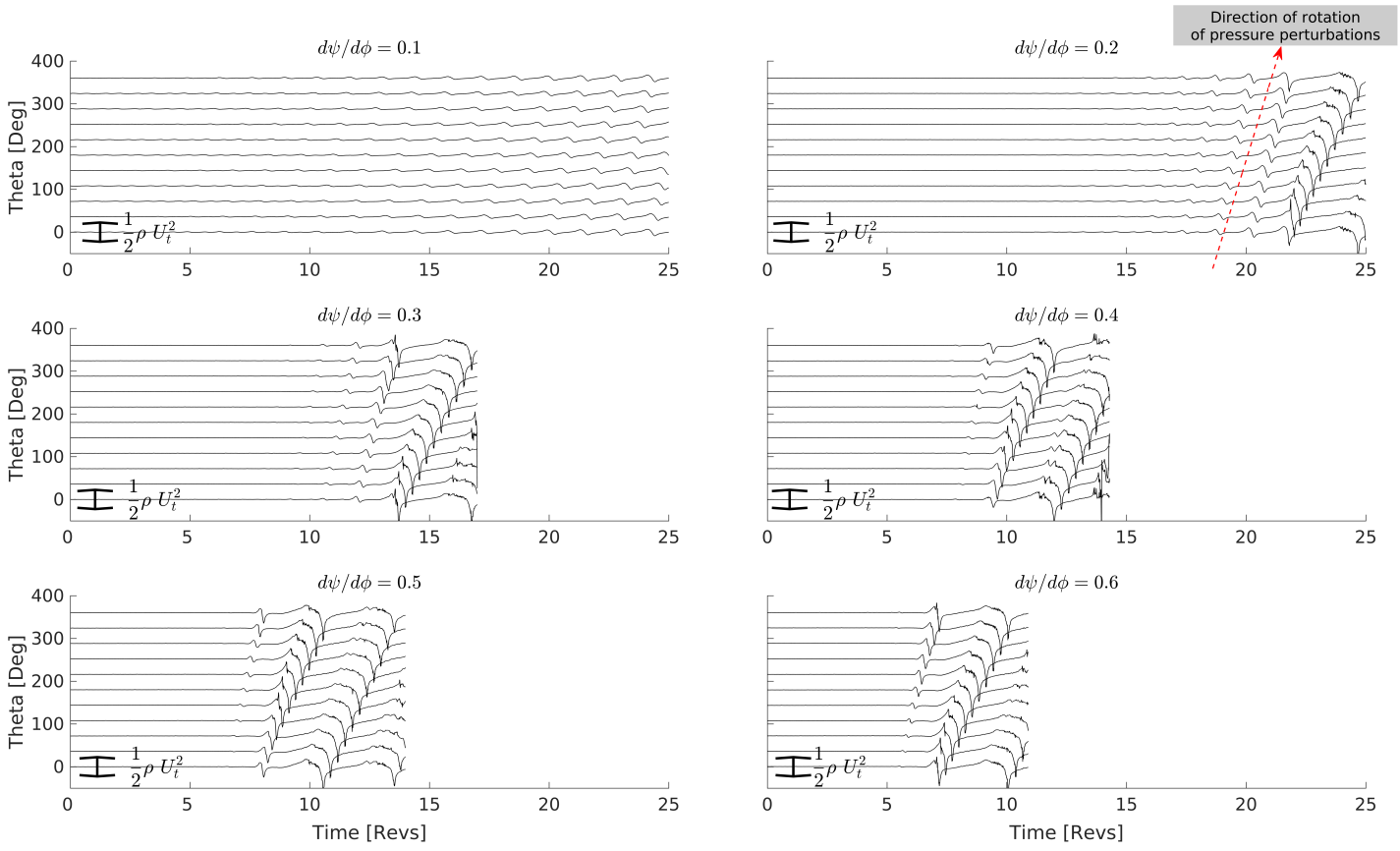

Figure 4.2: Time traces of pressure perturbations for rotating stall onset with characteristic slopes $d\psi^{TS}/d\phi$ from 0.1 to 0.6, at 11 circumferential locations.

4.1.1 Growth Rate of Perturbations During Stall Inception

To further illustrate the trends in Figure 4.2, Figure 4.3 shows the inverse of the growth rate, σ^{-1}, of the perturbations as a function of characteristic slope for a wider range of values of slope, from $d\psi/d\phi = 0.05$ to 3.0. The perturbation growth rate, defined in Section 2.1.1, was calculated from a linear fit of the first harmonic from the spatial Fourier decomposition of the rotor disk face pressure perturbations. Within the stall inception regime, these perturbations exhibit exponential growth. The details of the method of computing the perturbation (stall cell) growth rate are described in the Appendix in Section A.1.

Figure 4.3 shows a continuum of possible paths to stall, with an increase in the characteristic slope correlating with the increase in stall cell growth rate. This is consistent with the suggestion that the slope of the compressor pressure rise characteristic, $d\psi/d\phi$, is key in determining the behavior of rotating stall inception [8], [9].

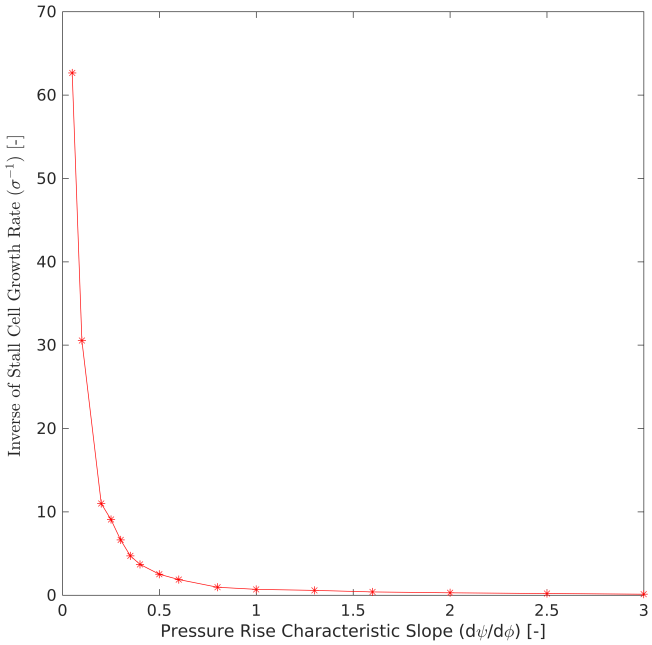

Figure 4.3: Growth rate of a stall cell during inception calculated for a characteristic slope range of $d\psi/d\phi = 0.05$ to 3.0, including both blade restagger and blade passage inertia.

4.2 Characteristics of a Continuum of Stall Inception Routes

4.2.1 Growth rate and Combination of Pressure Perturbation Harmonics

Figure 4.4 shows the magnitude of the spatial Fourier coefficients (SFCs) for the first six harmonics of the pressure perturbations of each case from Figure 4.2, where the black dashed lines indicate the stall inception regime[2]. Linear theory states that all harmonics become unstable at the same operating point, the peak of the compressor characteristic. The growth rates, σ_n, behave as $1/(\lambda_{rotor} + 2/n)$, where n is the harmonic number, and λ_{rotor} is the inertial parameter for the rotor defined by Equation 2.2.

For $d\psi/d\phi = 0.1$[3] and 0.2, the relative magnitude of the SFCs of the harmonics is time dependent, with the first and second order harmonics being the largest at the beginning of the stall inception regime. With increasing characteristic slope, the difference in size between the lower and higher harmonics decreases as seen in the final case, where $d\psi/d\phi = 0.6$. From Equation 2.8, the blade passage inertia decreases the growth rate of a given harmonic by a factor of $1 + \lambda_{rotor}\frac{n}{2}$.

Figure 4.4 indicates that at the beginning of the stall inception regime, for shallower sloped cases, the magnitudes of the SFCs for lower order harmonics are greater than higher order harmonics. All harmonics become unstable at the same operating point but their size relative to the mean flow differs, so the growth of higher harmonics is not initially visible due to the scale of the plot (resulting in separation between harmonics at shallower slopes). For smooth oscillatory perturbations like modal stall inception, the SFCs of lower order harmonics will be greater in magnitude because the perturbation is more sinusoidal compared to spike-type stall inception. Further reasoning behind this difference is given in

[2]The stall inception regime is defined in Section 2.1.1

[3]The beginning of the stall inception regime for $d\psi/d\phi = 0.1$ occurs two rotor revolutions earlier than the initial time on the SFC plot but is not included to maintain consistent scaling between all cases

Section A.2 in Appendix A.

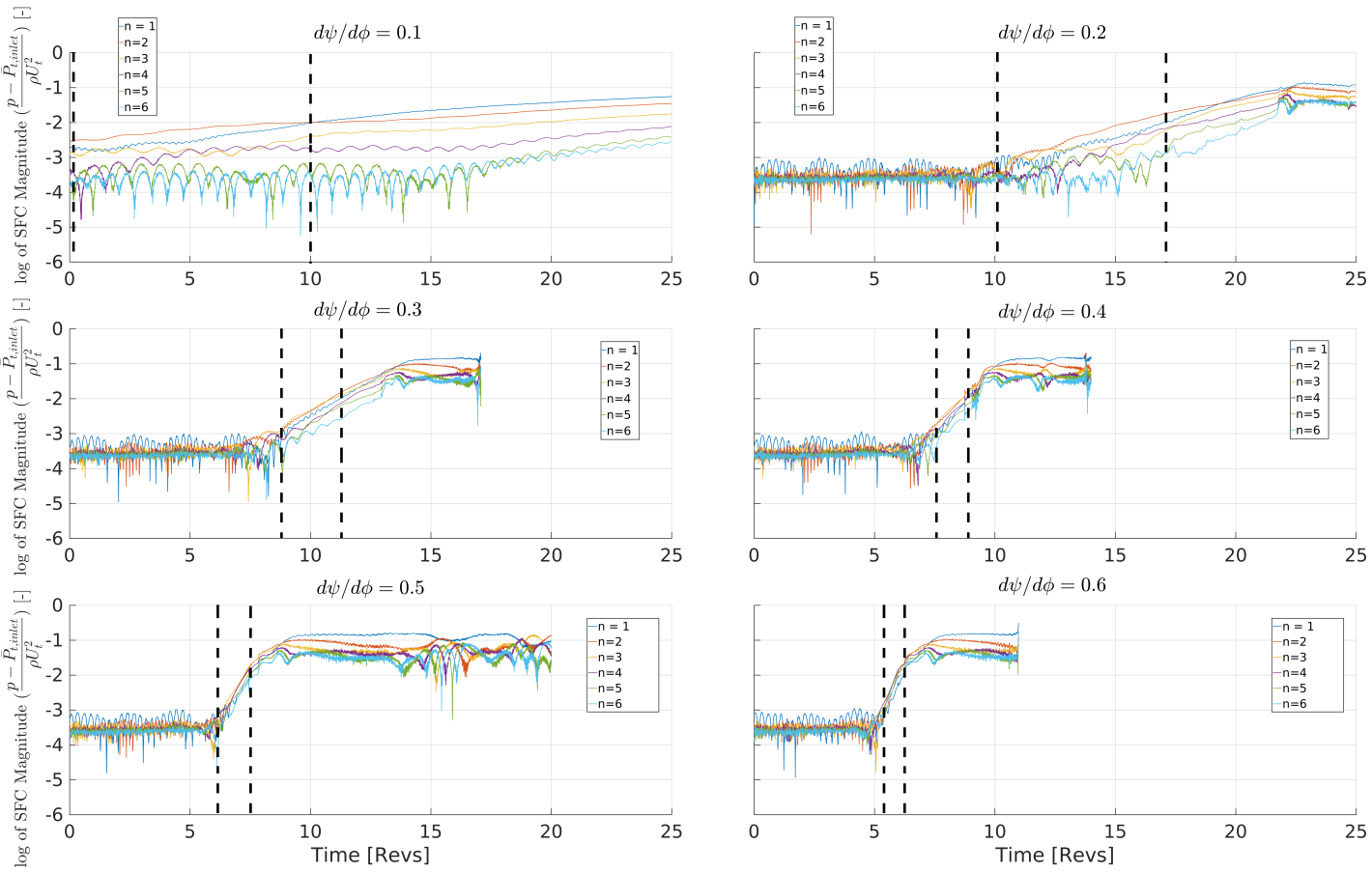

Figure 4.4: SFC plots of rotating stall for $d\psi/d\phi = 0.10$ to 0.60. Black dashed lines indicate the rotating stall inception regime.

4.2.2 Transient Behavior of the Rotor Operating Point During Stall Inception

Figure 4.5 and Figure 4.6 show the *local operating points* for the 101 circumferential and 7 radial points on the actuator disk at three separate times for the shallowest and the steepest characteristic slope case from Figure 4.2 ($d\psi/d\phi = 0.1$ and 0.6), respectively. The plot of the local operating points is referred to as the "orbit" of the rotor.

Figure 4.5 shows orbits for $d\psi/d\phi = 0.10$, and Figure 4.6 shows orbits for $d\psi/d\phi = 0.60$, both overlaid on the rotor axisymmetric characteristic. For both figures, the first time instant is the first observation of rotating stall, Figure 2.2, with little variation in flow around the rotor at the peak of the characteristic. Part of the rotor circumference encounters the positive side of the characteristic due to the restagger, resulting in growth of the perturbations. All radial stations have the same axisymmetric characteristic so the pressure rise, ψ^{TS}, across the actuator disk varies by 0.0002 from hub to tip. The subsequent plots show variation in the flow operating point within the stall inception regime. Figure 4.5 shows an increase in circumferential variation of the flow, but no noticeable radial variation over the course of 25 rotor revolutions while the stall cell grows. The operating points for the $d\psi/d\phi = 0.60$ case, seen in Figure 4.6, however, vary both circumferentially and radially. At 30.75 rotor revolutions, the $r^* = 0.667$ and 0.500 stations are further down the positive rotor characteristic than the $r^* = 1.00$ station, suggesting three dimensional flow. The stall inception regime is under two rotor revolutions, indicating spike-type stall.

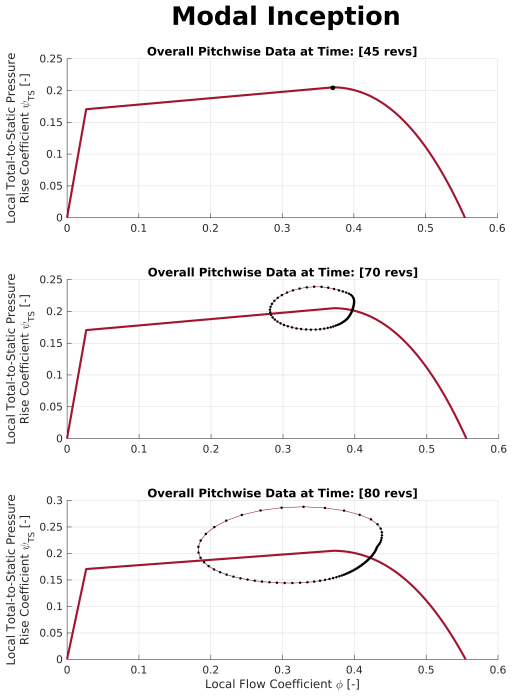

Figure 4.5: Mode-like stall inception. Orbits at three different times for the $d\psi/d\phi = 0.1$ case.

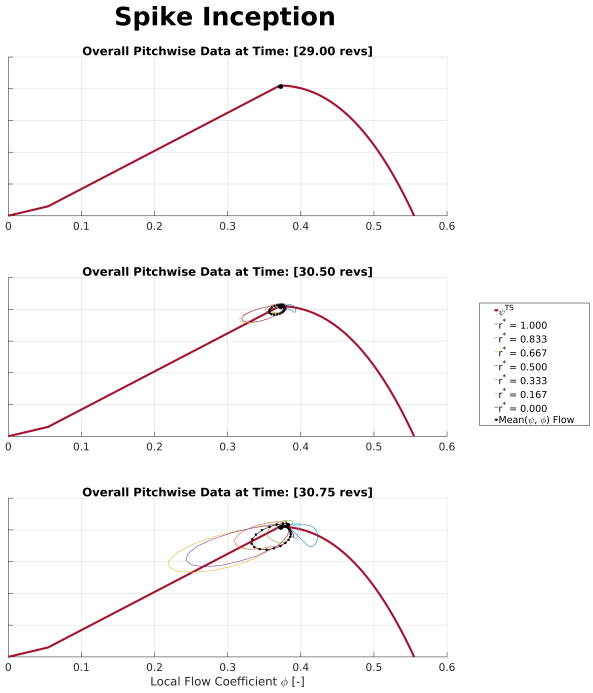

Figure 4.6: Spike-like stall inception. Orbits at three different times for the $d\psi/d\phi = 0.6$ case.

4.3 The Impact of Blade Passage Inertia and Blade Restagger on Stall Inception

This section considers the effects of parameters other than the characteristic slope: blade restagger[4] and blade passage accelerations (inertia). The same six characteristic slope cases as in Figure 4.2 are examined, first without restagger, and then without inertia.

Figure 4.7 shows pressure perturbations for a slope, $d\psi/d\phi$, $= 0.2$. The flow becomes unstable at the same operating point as in Section 2.2, the peak of the rotor characteristic, for all cases. The red dashed lines indicate the stall inception regime, based on the SFC decomposition (see Figure A.3 in the Appendix). The case without blade passage inertia has the fastest growth rate and the pressure traces appear spike-like. The stall inception regime[5] for the case with inertia, but without restagger, begins over four rotor revolutions later than the other two cases.

[4] see definition of restagger in Section 2.1.5
[5] defined in Section 2.1.1

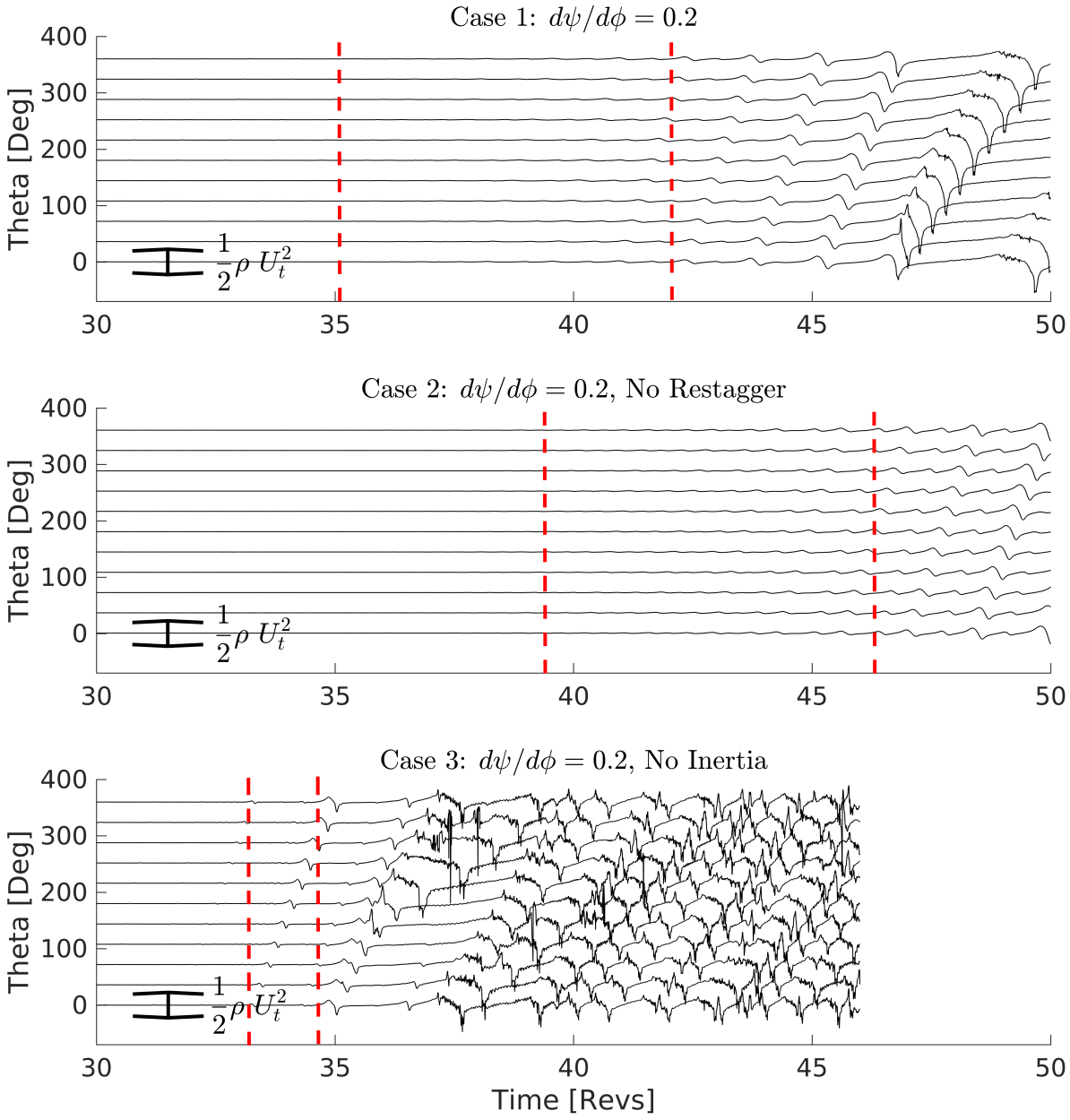

Figure 4.7: $d\psi/d\phi = 0.2$ case showing pressure traces for each case: Case 1) Includes blade restagger and blade passage inertia. Case 2) Includes inertia but not restagger. Case 3) Includes restagger but not inertia. The red dashed lines mark the stall inception regime.

4.3.1 The Effect of Blade Passage Inertia

Increases in the blade passage inertia reduce the growth rate of the stall cell [10]. Figure 4.8 compares the $d\psi/d\phi = 0.2$ case with inertia to the one without inertia, showing the slower growth rate for the former. The extent of the stall inception regime is indicated by red dashed lines. There a greater difference in magnitude between the SFCs of lower order and higher order harmonics within the stall inception regime for the case with blade passage inertia. The opposite is true for the case without blade passage inertia, which was noted in Section 4.2.1 as behavior associated with spike-like disturbances.

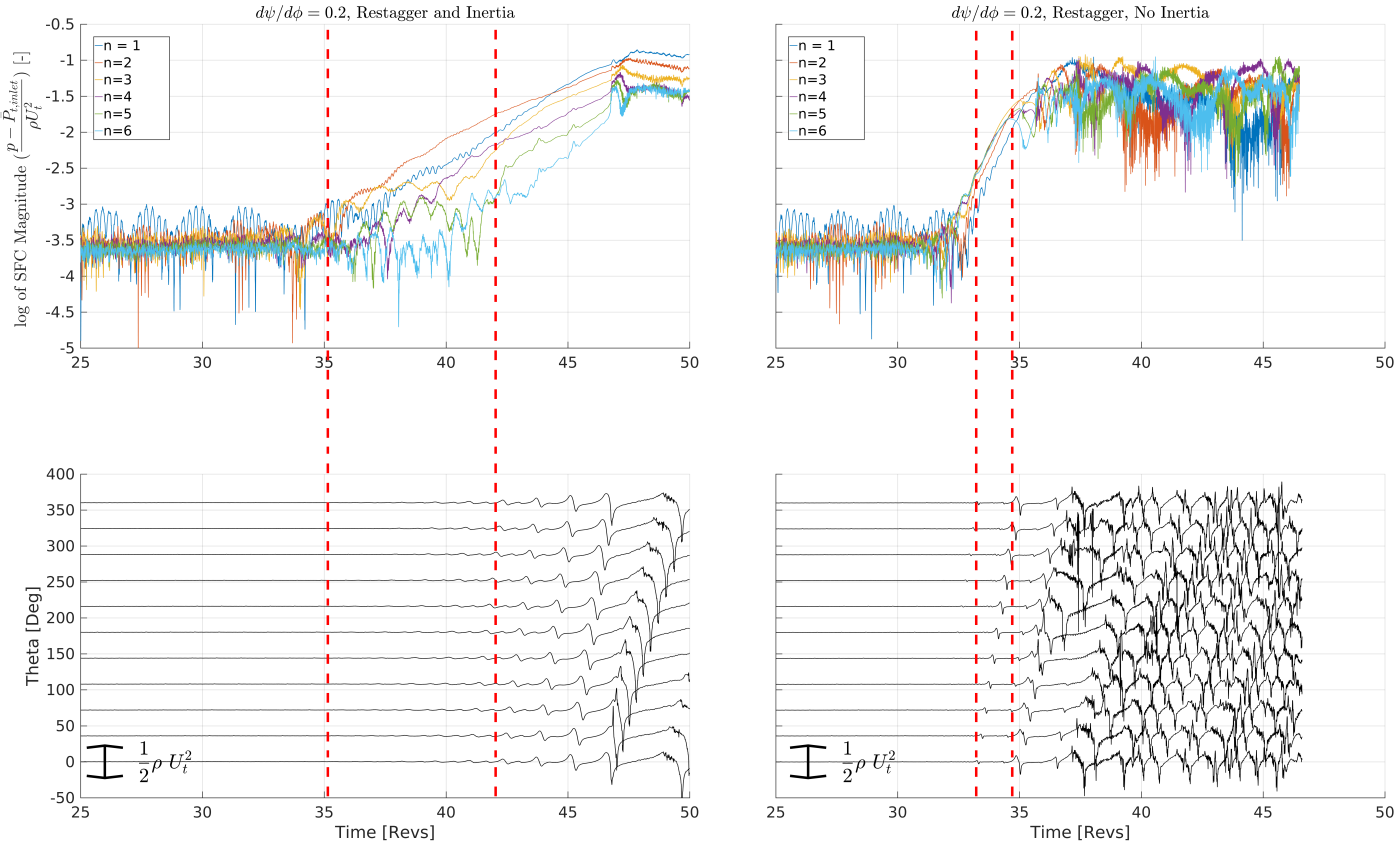

Figure 4.8: $d\psi/d\phi = 0.2$ characteristic slope case with inertia (left) versus without inertia (right).

Figure 4.10 provides growth rates, for six cases without blade passage inertia, as a function of rotor characteristic slope. As in Figure 4.3, there is a hyperbolic-like relationship between the inverse of the growth rate of pressure perturbations and characteristic slope, suggesting that the continuum of stall inception routes exists independent of the presence of blade passage inertia.

4.3.2 The Effect of Blade Restagger

As discussed in Section 2, stall inception begins when the localized operating point at the actuator disk is moved to the positively sloped part of the pressure rise characteristic. For axisymmetric flow, however, the rotor cannot enter into rotating stall, because, from the set up of TBLOCK, there is no asymmetry. (The role of asymmetric restagger in initiating rotating stall in TBLOCK is further discussed in Section C.1 in the Appendix.)

Figure 4.9 compares the $d\psi/d\phi = 0.2$ case with blade restagger to that without blade restagger. The stall inception region is indicated by red dashed lines. The case on the left includes the 0.1° RMS restagger. Prior to stall inception, the SFC plot shows oscillatory beating of the first harmonic due to the restagger; without restagger, the first harmonic is irregular prior to stall inception. Both cases become unstable at the same operating point, but the case without restagger reaches the beginning of the stall inception regime 4.3 rotor revolutions later than the case with restagger. For a case with a shallower characteristic slope and hence mode-like behavior, the growth rate may be slow enough that any pre-existing asymmetries are amplified. The SFCs in Figure 4.9 show that the pressure perturbations prior to stall inception are approximately an order of magnitude larger with restagger than for without. If both cases have the same growth rate, the case with the smaller initial perturbation will reach the stall inception regime at a later time.

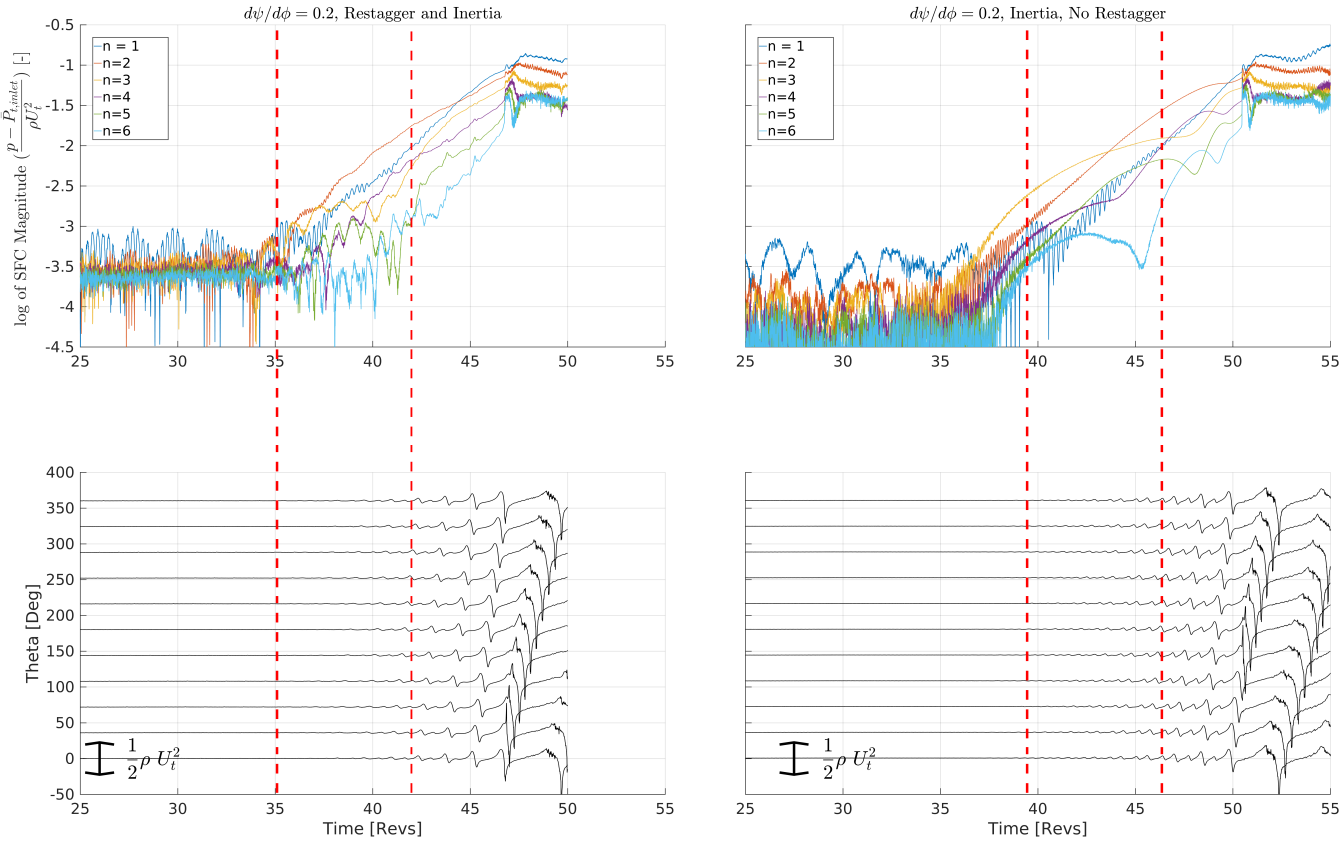

Figure 4.9: $d\psi/d\phi = 0.2$ characteristic slope case with asymmetric restagger (left) and without restagger (right).

Figure 4.10 shows the inverse of the growth rate of pressure perturbations as a function of the positive characteristic slope for $d\psi/d\phi = 0.1$ to 0.6. The three lines show the situations with both asymmetric restagger and blade passage inertia, inertia but not restagger, and restagger but not inertia. The same trend in growth rate (increasing growth rate with increasing characteristic slope) is observed for all three cases, suggesting it exists regardless of the presence of blade passage inertia or restagger.

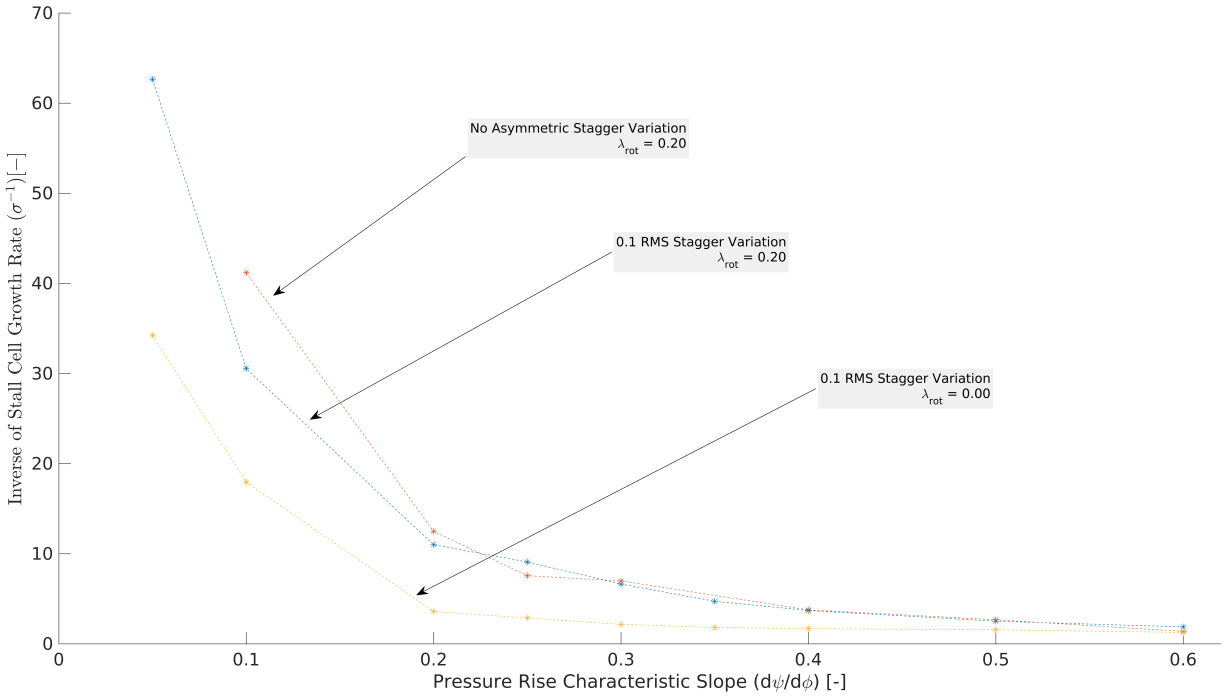

Figure 4.10: Inverse of pressure perturbation growth rate, σ, within the stall inception regime for a pressure rise characteristic slope, $d\psi/d\phi = 0.1$ to 0.6, for three cases. Case 1) Includes blade restagger and blade passage inertia. Case 2) Includes inertia but not restagger. Case 3) Includes restagger but not inertia.

4.4 Comparison of TBLOCK Results and Two-Dimensional Linear Theory

The growth rate trends seen within this chapter imply that modal and spike stall inception exist at opposite ends of a spectrum of paths to rotating stall, consistent with the results of Pullan and Logrono [8], [9]. (Logrono's simulation set up differed from what was used here, however and this difference is described in Appendix A.3). To provide a baseline for the applicability of linear theory to the simulated rotating stall cases, the growth rate expression, Equation 2.8, for the first harmonic is compared to the growth rate from TBLOCK in Figure 4.11.

Cases without blade passage inertia have the largest growth rates. The growth rate for the cases with and without restagger are nearly equivalent for characteristic slopes $d\psi/d\phi \leq 0.4$. For cases with inertia, the growth rate predicted by TBLOCK for $d\psi/d\phi \leq 0.3$ agrees well with linear theory. The divergence of TBLOCK simulated growth rates from theory as the characteristic slope is increased indicates that stall inception can no longer be described by two-dimensional theory for $d\psi/d\phi > 0.3$. This is further discussed in Section 4.5 below. This divergence of the growth rate predicted by TBLOCK from theory at a slope of 0.3 was also noted by Logrono [8].

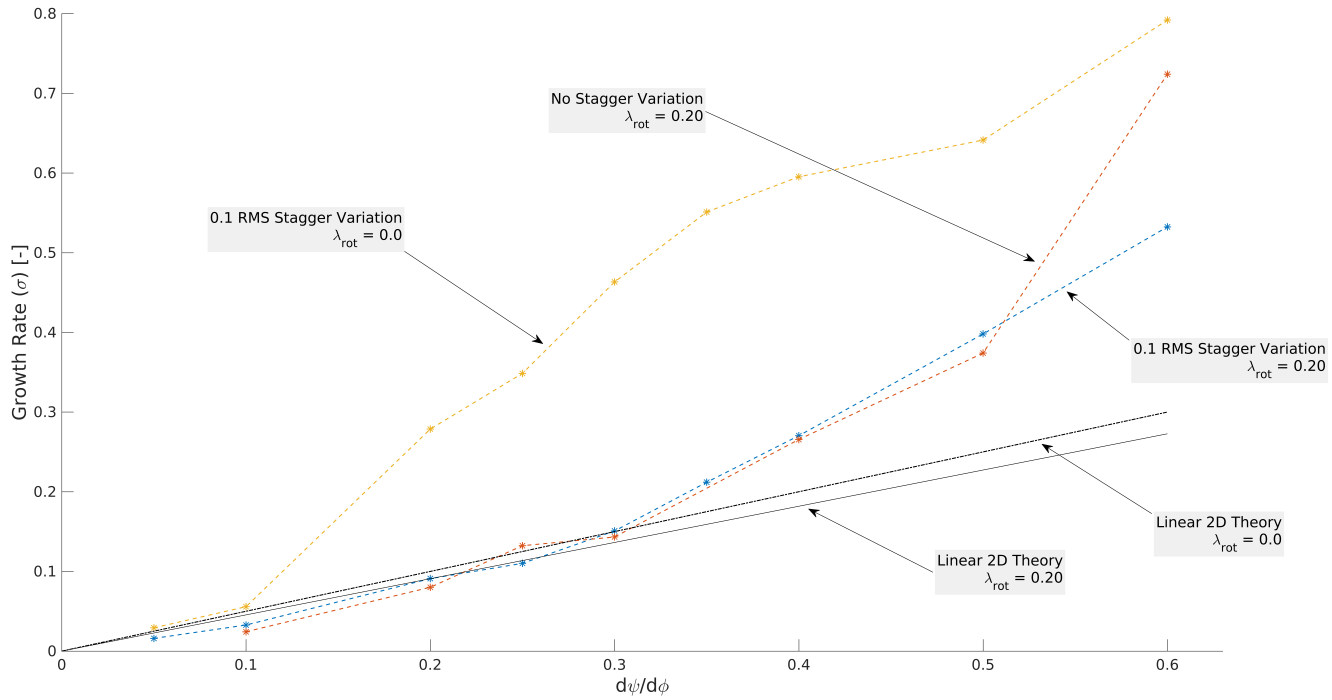

Figure 4.11: Comparison of the growth rates for three cases for slopes from $d\psi/d\phi = 0.05$ to 0.6. Case 1) Includes blade restagger and blade passage inertia. Case 2) Includes inertia but not restagger. Case 3) Includes restagger but not inertia. The straight black lines show the growth rate predicted by two dimensional linear theory.

4.5 Investigation of the Divergence of Stall Inception from Two-Dimensionality for an Isolated Rotor

The linear theory that has been discussed is based on a two-dimensional stall model. The geometry used in the TBLOCK calculation has a high HTR of 0.9999 such that the isolated rotor is close to a 2D cascade and Laplace's equation implies that perturbations in the axial and circumferential directions are of the same order. Observations in Section 4.2 and Section 4.4, however, show that the stall inception cannot be assumed to be two-dimensional with steeper characteristic slopes.

Figure 4.12 gives the orbits for the six cases of Figure 4.2, at a time halfway through the stall inception regime. The shallower sloped cases, $d\psi/d\phi \leq 0.3$, in Figure 4.12, exhibit two-dimensional growth. The steeper sloped cases show radial variation in the local operating points of the rotor. This is elaborated upon in Section 4.5.1. This suggests that three-dimensional growth of disturbances in the flow during stall inception correlates to spikes, whereas modal stall inception is purely two-dimensional.

4.5.1 Departure from 2D as a Function of Characteristic Slope

Figure 4.13 shows the divergence of stall inception from two-dimensionality as a function of $d\psi/d\phi$. The ratio of the root mean square (RMS) of the radial velocity perturbations to the RMS of the axial velocity perturbations, $\frac{RMS(\delta V_r)}{RMS(\delta V_x)}$, are compared at a time halfway through the stall inception regime. For a positive slope $d\psi/d\phi$ below 0.3, $\frac{RMS(\delta V_r)}{RMS(\delta V_x)} \leq 0.1$ at all radial stations, i.e. the radial perturbations are an order of magnitude smaller than the axial and circumferential perturbations during stall inception. For slopes $d\psi/d\phi$ above 0.3, there is an increase in $\frac{RMS(\delta V_r)}{RMS(\delta V_x)}$ at all radial stations. For $d\psi/d\phi = 0.35$, $\frac{RMS(\delta V_r)}{RMS(\delta V_x)} = 2.5$ at the $r^* = 1.000$ station, indicating a transition between quasi-two-dimensional, and three-dimensional flow for stall inception that is dependent on the compressor pressure rise characteristic. Figures

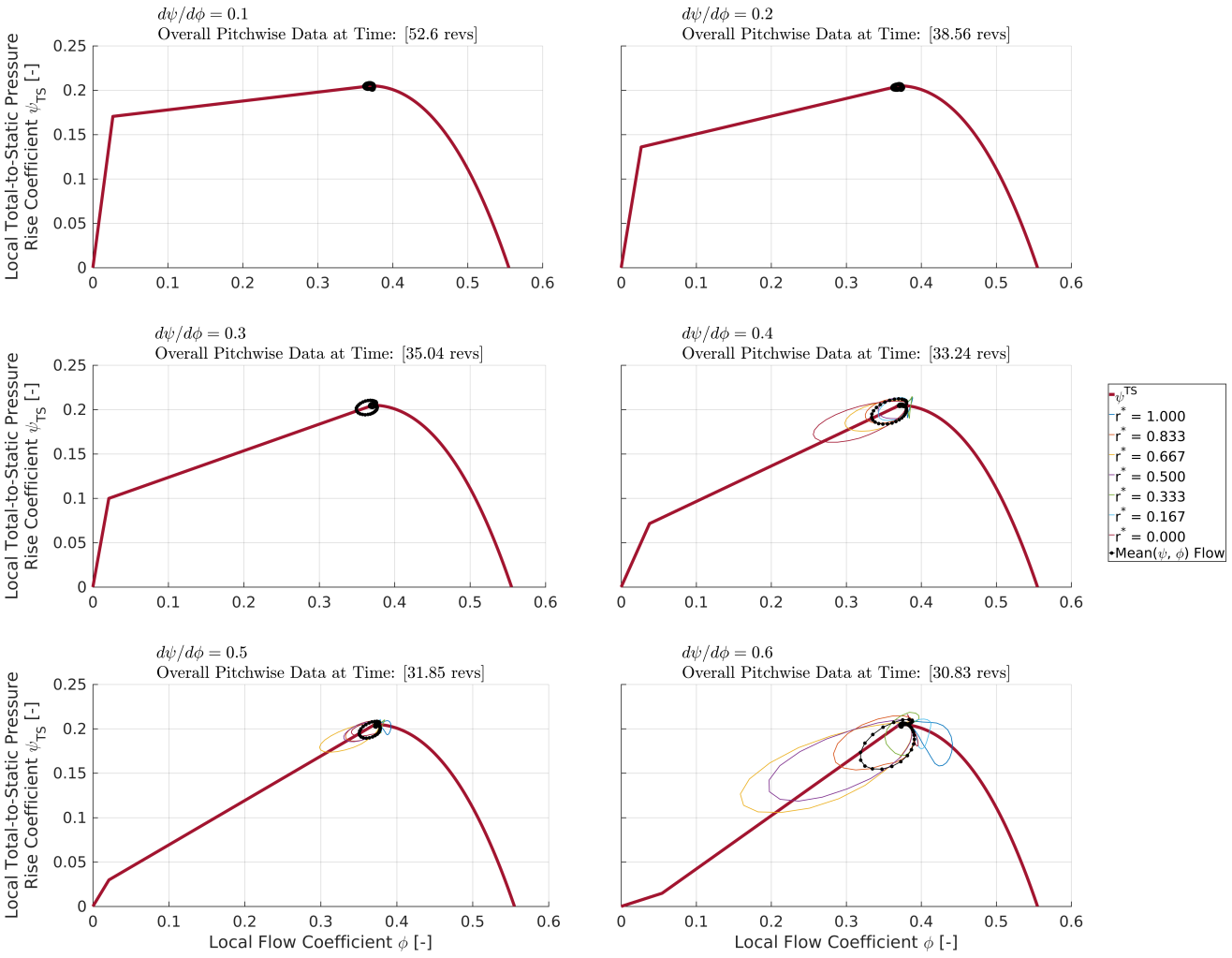

Figure 4.12: Orbits for $d\psi/d\phi = 0.1$ to 0.6 at a single point in time during stall inception. The thick dark red line is the axisymmetric compressor characteristic, the black dotted line is the radially averaged mean flow at each circumferential point around the annulus, and the local flow at the seven radial stations is plotted using the following colors: $r^* = 0.000$ dark red, $r^* = 0.167$ light blue, $r^* = 0.333$ green, $r^* = 0.500$ purple, $r^* = 0.667$ yellow, $r^* = 0.833$ orange, $r^* = 1.000$ dark blue.

D.2 in the Appendix provide additional evidence for this transition. Further, the departure from quasi-two-dimensional flow at $d\psi/d\phi = 0.3$ agrees with the divergence of the growth rate of the perturbations from TBLOCK simulations from two-dimensional theory as observed in Figure 4.11.

The RMS of the axial, tangential and radial velocity perturbations for $d\psi/d\phi = 0.3$ and 0.4 is compared in Figures 4.14 and 4.15. Within the stall inception regime, the three velocity perturbations are of the same order of magnitude in the steeper slope case. The radial variation in both the axial and tangential velocity perturbations indicates three-dimensional flow.

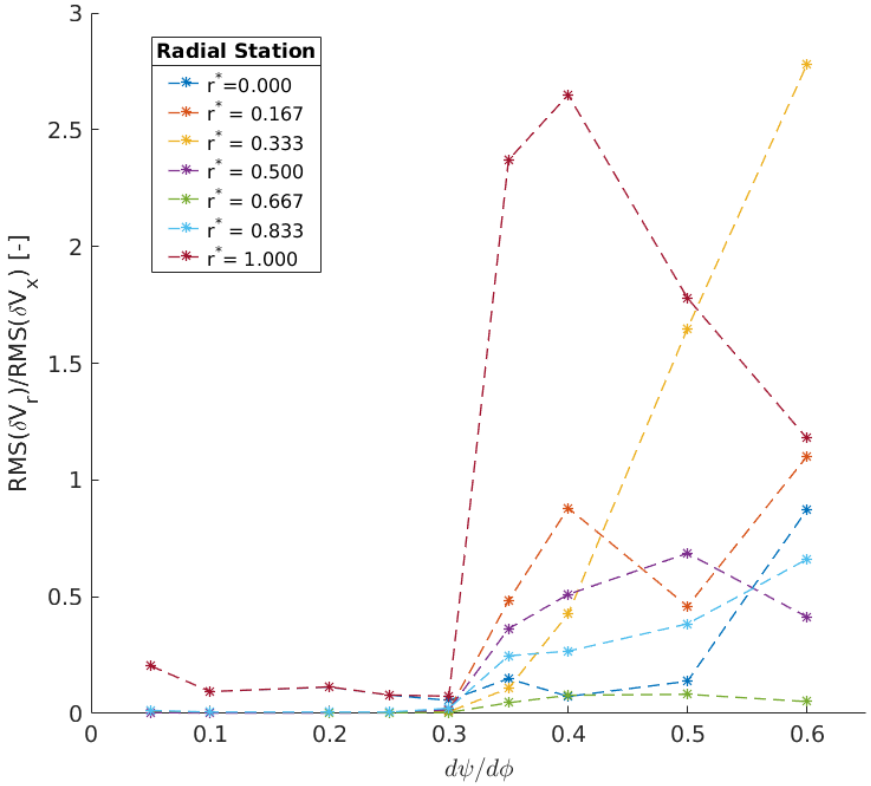

Figure 4.13: Ratio of RMS of radial to axial velocity perturbations as a function of compressor characteristic slope. The ratio at the seven radial stations is plotted using the following colors: $r^* = 1.000$ dark red, $r^* = 0.833$ light blue, $r^* = 0.667$ green, $r^* = 0.500$ purple, $r^* = 0.333$ yellow, $r^* = 0.167$ orange, $r^* = 0.000$ dark blue.

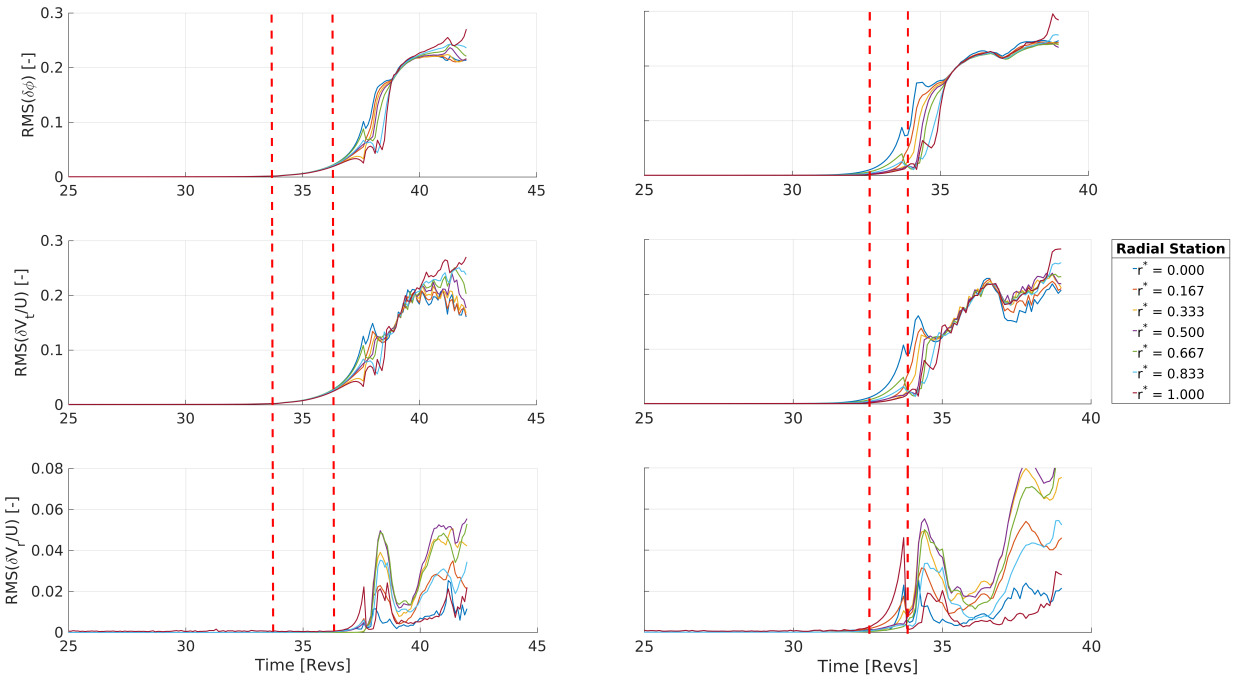

((a)) $d\psi/d\phi = 0.3$ ((b)) $d\psi/d\phi = 0.4$

Figure 4.14: Velocity perturbations in the axial, tangential and radial direction for a characteristic slope of 0.3 and 0.4. Red dashed lines identify the stall inception regime. The local perturbations at the seven radial stations are plotted using the following colors: $r^* = 1.000$ dark red, $r^* = 0.833$ light blue, $r^* = 0.667$ green, $r^* = 0.500$ purple, $r^* = 0.333$ yellow, $r^* = 0.167$ orange, $r^* = 0.000$ dark blue.

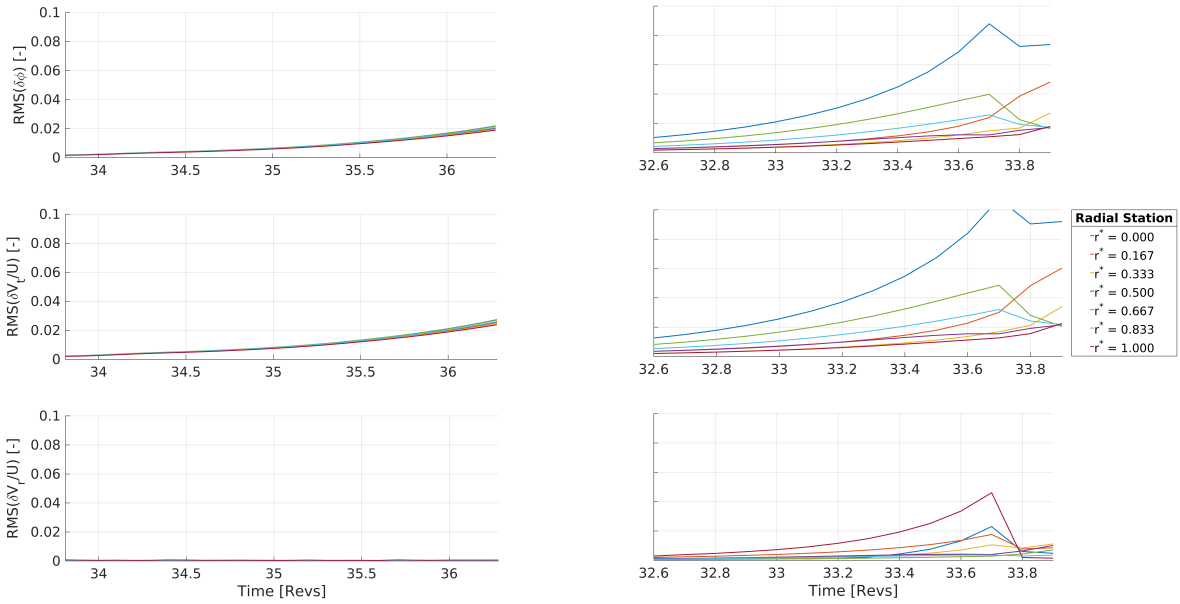

((a)) $d\psi/d\phi = 0.3$ ((b)) $d\psi/d\phi = 0.4$

Figure 4.15: Velocity perturbations in the axial, tangential and radial direction for a characteristic slope of 0.3 and 0.4. The time span is only the stall inception regime. The local perturbations at the seven radial stations are plotted using the following colors: $r^* = 1.000$ dark red, $r^* = 0.833$ light blue, $r^* = 0.667$ green, $r^* = 0.500$ purple, $r^* = 0.333$ yellow, $r^* = 0.167$ orange, $r^* = 0.000$ dark blue.

4.5.2 Effects of Blade Passage Inertia and Blade Restagger on the Departure of Stall Inception From 2D

Figure 4.16 compares the orbits taken at a time halfway through the stall inception regime for $d\psi/d\phi = 0.2$ without blade restagger and without blade passage inertia. There is no local radial variation of flow for these cases.

The value of $\frac{RMS(\delta V_r)}{RMS(\delta V_x)}$ as a function of characteristic slope is shown in Figure 4.18 and Figure 4.17 for runs without blade restagger, and without blade passage inertia, for a time halfway through the stall inception regime. The divergence of the flow from two-dimensionality at $d\psi/d\phi = 0.3$, is observed for both cases, suggesting that the occurrence of the transition from quasi-two-dimensional to three dimensional flow does not depend on the presence of blade restagger and blade passage inertia. There is currently no explanation for the drop of $\frac{RMS(\delta V_r)}{RMS(\delta V_x)}$ at a slope of $d\psi/d\phi = 0.6$. This should be addressed in future work.

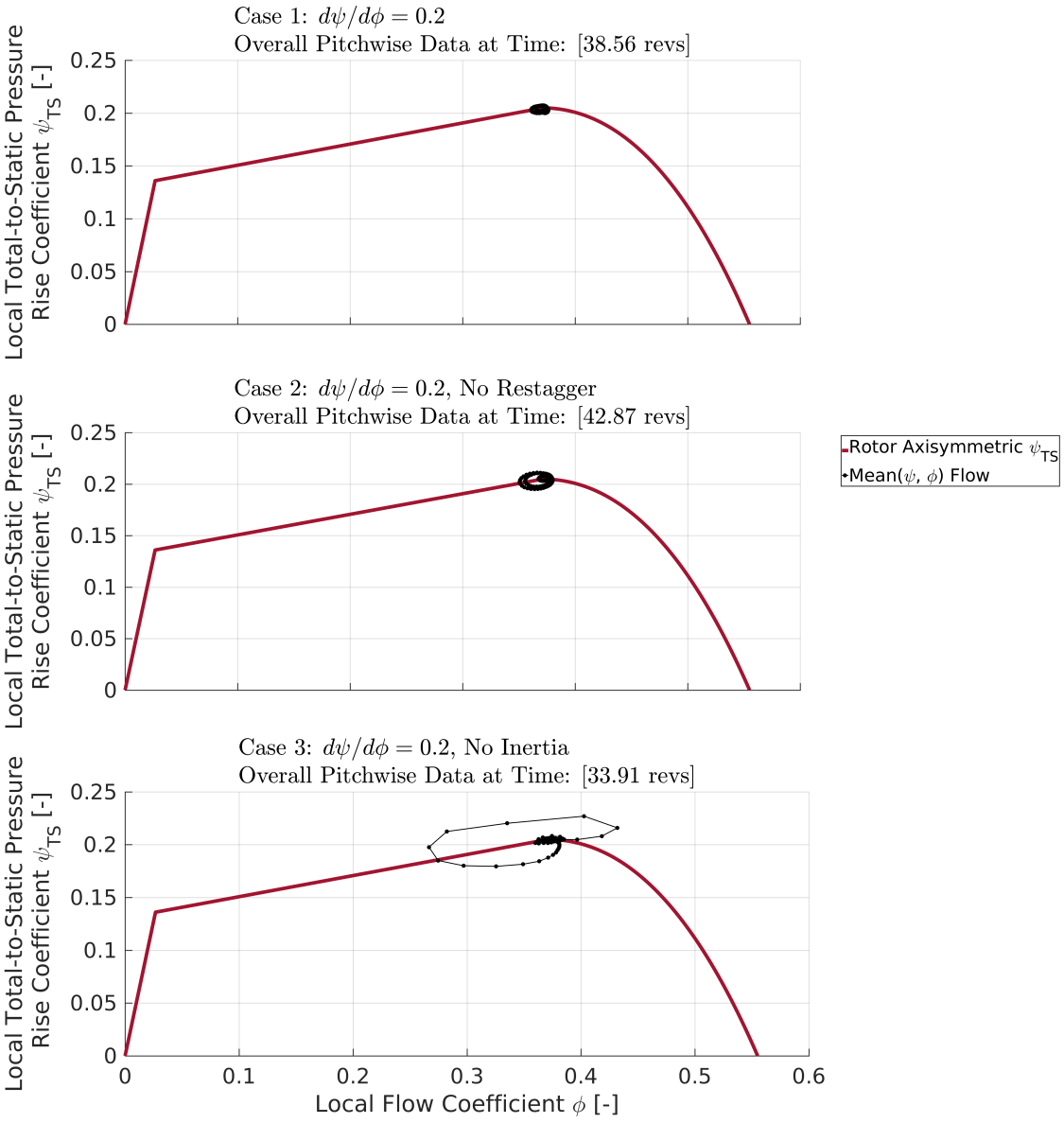

Figure 4.16: Plot of the radially averaged flow operating points on the axisymmetric compressor pressure rise characteristic for $d\psi/d\phi = 0.2$. 1) Case with blade restagger and blade passage inertia 2) Case with inertia, but without restagger 3) Case with restagger, but without inertia.

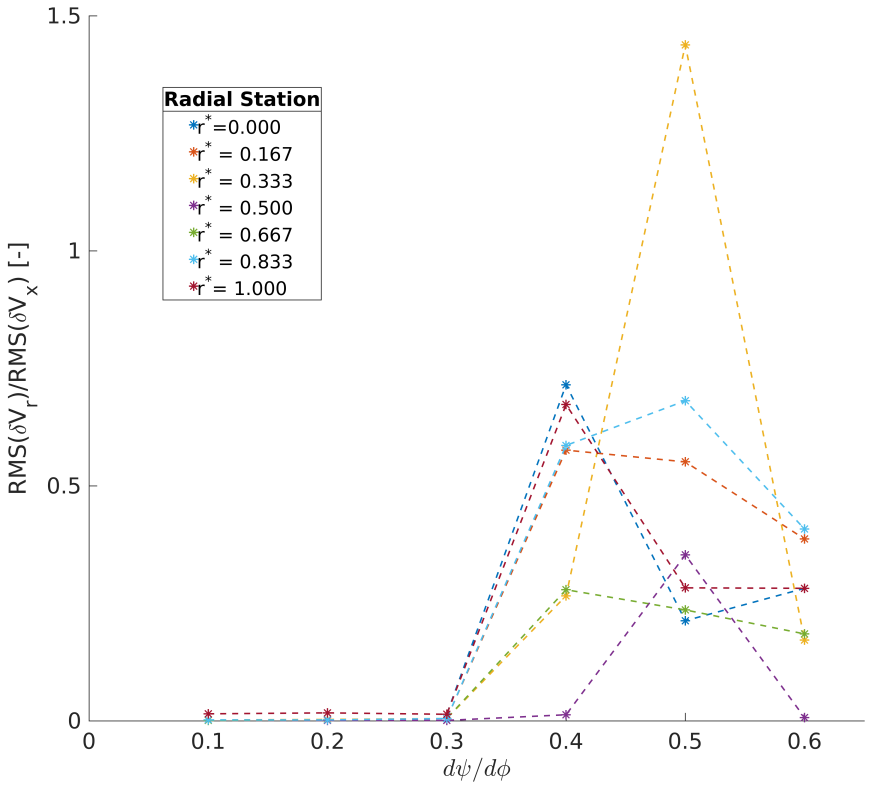

Figure 4.17: Ratio of RMS of radial to axial velocity perturbations as a function of compressor characteristic slope, without inertia. The ratio at the seven radial stations is plotted using the following colors: $r^* = 1.000$ dark red, $r^* = 0.833$ light blue, $r^* = 0.667$ green, $r^* = 0.500$ purple, $r^* = 0.333$ yellow, $r^* = 0.167$ orange, $r^* = 0.000$ dark blue.

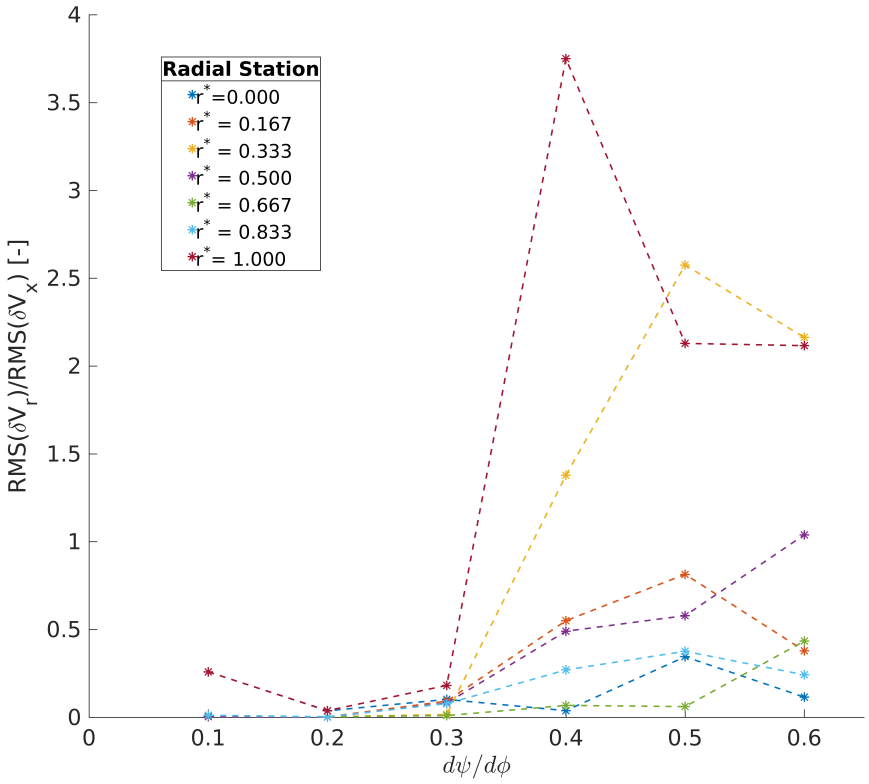

Figure 4.18: Ratio of RMS of radial to axial velocity perturbations as a function of compressor characteristic slope, without restagger. The ratio at the seven radial stations is plotted using the following colors: $r^* = 1.000$ dark red, $r^* = 0.833$ light blue, $r^* = 0.667$ green, $r^* = 0.500$ purple, $r^* = 0.333$ yellow, $r^* = 0.167$ orange, $r^* = 0.000$ dark blue.

4.6 Characterization of Modal and Spike Stall as Past of a Continuum

The mode-spike continuum identified in Section 4.1 implies that modal and spike stall can be considered as "ends" of a continuum of possible paths to stall, consistent with other observations made by the MIT-Cambridge team [9]. The most important parameter that determines the behavior of the path to stall is the positive gradient of the compressor pressure characteristic at flows below the peak pressure rise, and blade passage inertia and blade restagger do not affect the general trends. Modal-type stall inception occurs for shallow characteristic slopes, $d\psi/d\phi \leq 0.1$, with the growth rates agreeing with linear theory. Spike-type stall inception is associated with three-dimensional behavior. Based on the calculations carried out, other paths have features associated with both spike and modal stall inception. For the isolated rotor examined, stall inception develops features associated more with spike stall than with modal stall at $d\psi/d\phi \approx 0.3$, in agreement with the observations of Logrono [8].

Chapter 5

Conclusion

5.1 Summary and Conclusions

An investigation has been carried out to redefine mode and spike stall inception based on rotating stall calculations performed with the TBLOCK/actuator disk method. The following learnings are presented from this work:

1. The hypothesis of a stall inception continuum, and the unification of modes and spikes as part of the same dynamical framework, was born out of the calculations carried out. Modal inception and spike inception should be considered two stall inception scenarios that are located on opposite ends of the continuum of possible paths to stall. Other paths to stall inception on this this continuum have features associated with both spike and modal stall.

2. For an isolated rotor with blade restagger and inertia, stall inception begins to develop features associated with spike stall rather than modal stall at $d\phi/d\phi \approx 0.3$. This agrees with observations made by Logrono [8].

3. For the isolated rotor examined, the key determinant of the path to stall is the positive gradient of the compressor pressure rise characteristic at flows below the peak pressure. Inertia and restagger do not affect the general trend of the continuum.

4. The stall cell growth rate from linear, two-dimensional analysis generally agrees with that from the TBLOCK/actuator disk simulations for characteristic slopes $d\phi/d\phi \leq 0.3$, for cases with or without blade passage inertia and blade restagger.

5. For the calculations carried out with slopes greater than 0.3, there was a departure of stall inception from two-dimensionality and thus a departure from its agreement with 2D theory, showing that the spike stall inception that was encountered was three-dimensional, although previous URANS calculations have shown that three-dimensionality is not necessary for spike stall [6].

5.2 Recommendations

This thesis focused on stall inception routes as a function of the positive slope of the compressor pressure rise characteristic, and only that part of the compressor characteristic was varied. Analysis of the stall inception route for characteristics with other shapes, including variation of the negatively sloped part of the characteristic should also be considered. Simulations should also be run with loss lag effects to see how they impact stall inception and the trends observed. Further modeling should also be done with a lower HTR ratio case to see how this affects the two-dimensionality of stall inception at shallow characteristic slopes.

5.2.1 Current Work

It is emphasized that, at the time of this thesis, the MIT-Cambridge team is continuing its efforts to define, model, and understand rotating stall inception. None of the learnings contained within this thesis contradict current learnings and the work reported on is a snapshot of the progress being made by the collaborative Gas Turbine Lab, and Whittle Lab teams. The work in progress includes:

- Two expressions generated to describe rotating stall growth and rotation rates by Stenning and Spakovszky, have been successfully reconciled [3], [10].

- Rotating stall inception is being examined for cubic characteristics with varying height at the peak; this increases the gradient of the characteristic on both stable and unstable sides, and affects the growth and rotation rates.

- For lower HTR ratio cases, the positive slope for the axisymmetric characteristic is being varied radially to model spike and part span stall inception.

- Body force modeling is being used to simulate rotating stall.

- Stall cell rotation rate during inception from TBLOCK is being compared with updated expressions from linear theory.

- The relationship between the spatial Fourier decomposition required to describe stall inception as a function of characteristic slope is being conducted.

Part II

Concept Questions in Fluid Dynamics

Chapter 6

Generation of Concept Questions for Teaching and Learning Fluid Dynamics

A second aspect of this masters thesis encompasses the creation, editing, and compilation of Concept Questions for a textbook of fluid dynamic questions. Many of the examples are aimed at concepts and applications in propulsion and power generation (much of the material is taken from two MIT classes: 16.120 Compressible Internal Flow and 16.540 Internal Flows [14]), but the ideas are applicable to a broad range of fluid dynamic contexts. The questions are intended to be used in a classroom setting or as self study to further student conceptual understanding. This chapter discusses learnings taken from development of these questions, provides metrics for what could be considered a "good" concept question, and includes illustrations of the editing of questions to enhance accessibility and the connection to learning.

6.1 Importance of Conceptual Understanding

Conceptual understanding of a problem is key in allowing students to take learnings from an isolated setting (a classroom!) and apply them to real scenarios (i.e. scenarios without chapter headings to provide guidance towards the main ideas). To solve a problem, one must

be able to distinguish its parts, and identify and interpret the contributing factors [15]. The book is thus composed of questions that test fundamental understanding. Questions at the undergraduate or even graduate level can become predictable in their structure and answer. From a student perspective, in some instances, solving problems can rely more on pattern recognition than the application of knowledge to an open ended question. The Concept Questions being developed are meant to challenge student foundations and critical analysis; they can be approached from first principles and deconstructed into constituents to provide the solution through establishment of the principal assumptions and roots of the problem [15].

6.2 Creating "Good" Concept Questions

Concept Questions provide a means to assess one's knowledge of fundamentals, and enhance learning through testing and reflection. To create a Concept Question, the author must consider:

- The intellectual nugget[1], or learning, that is intended for the reader to grasp.
- The baseline knowledge expected of the reader prior to attempting the question.
- If the problem description give enough information to solve the question.
- What is to be gained from the question.

Creation of a *good* concept question requires features additional to those listed above. Clarity in asking a question reduces the likelihood of misinterpretation by the reader. It is also important to consider the wording of the question itself.

The Concept Question should have the following qualities[2]:

- Be based on direct application of a fluid dynamics principle or characteristic

[1] Termed coined by Professor J. L. Kerrebrock
[2] List is adapted from 16.120 Internal Flows class notes

- Be clear, and well communicated via a description and/or figure
- The question and answer served as analogies, springboards, to other situations
- Has an answer that can be stated simply and can be reasoned without calculation (or with simple calculation)
- The arguments (train of logic) for the answer often involved approximations – their validity has limitations
- The reader can clearly articulate the approximations and the limits
- The reader can define the concept(s) illustrated

6.2.1 Examples of Edited Questions

The four examples below illustrate how Concept Questions were improved through editing.

Question Rephrasing

The following question regarding a wind tunnel was reworded, addressing specifically the knowledge level of the audience.

Original Question

What is the minimum loss configuration for the supersonic wind tunnel sketched below? There may be more than one answer depending on the tunnel capabilities, e.g., variable area versus fixed area. If so, please define the capability that determines which answer is appropriate.

(a) No loss

(b) Loss corresponding to a shock at test section Mach number

(c) Loss corresponding to a shock at diffuser throat Mach number

(d) Some other value

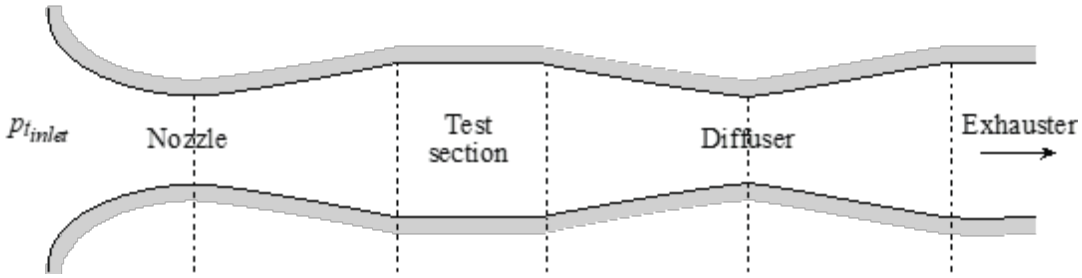

Figure 6.1: Starting of a supersonic wind tunnel from rest?

Editing Process

What is the minimum loss configuration for the starting of a supersonic wind tunnel sketched below i.e. running the tunnel with supersonic flow in the test section? ~~There may be more than one answer depending on the tunnel capabilities, e.g.,~~ Give the configuration for a wind tunnel with a variable area diffuser, and the configuration for a tunnel with a fixed area diffuser ~~versus fixed area.~~ If so, please define the capability that determines which answer is appropriate .

Updated Wording

*What is the minimum loss configuration for the **starting** of the supersonic wind tunnel sketched below, i.e., running the tunnel with supersonic flow in the test section? Give the configuration in terms of the ratio of diffuser throat area to nozzle area for a tunnel with a variable area diffuser, and for a tunnel with a fixed area diffuser. Please define the capability that determines which answer is appropriate.*

(a) No loss

(b) Loss corresponding to a shock at test section Mach number

(c) Loss corresponding to a shock at diffuser throat Mach number

(d) Some other value

The original wording of the question was obscure. The updated wording clarifies what is expected as an answer and provides context for those who may not know the general purpose of a supersonic wind tunnel. The description provides additional context, specifically that this question centers around the *starting* of a wind tunnel. For the reader who does not know the difference between supersonic, subsonic, and transonic wind tunnels, it states the desired operational requirement for the tunnel: that there be supersonic flow in the test section, relating the problem statement to Figure 6.1.

Updating a Figure

The figure for a question can be as important as the problem statement in preventing misinterpretation. It can also provide visual aid, which is crucial when describing scenarios that have not been encountered by the reader before. For the following two questions, figures were updated to improve question comprehension and clarity.

Figure 6.2 and Figure 6.3 show the before and after for a question regarding a jet aircraft. The addition of the internal control volume and updated tail for the aircraft provides additional context for the question.

Question [Adapted from Shapiro and Sonin, 2010]

A jet aircraft has an engine nozzle that can swivel from pointing straight downstream, as in horizontal flight, to upstream, i.e., over a range of 180 degrees in the angle, shown below, between the direction of the jet and the horizontal. The engine inlet is indicated.

(a) For the aircraft to hover, what should be the value of the nozzle angle θ?

(b) If the mass of the aircraft is M, the mass flow rate through the jet engine is $\dot{m}$, and the exhaust is ideally expanded (exit pressure equal to atmospheric pressure), what is the velocity at the exit of the nozzle during hover?

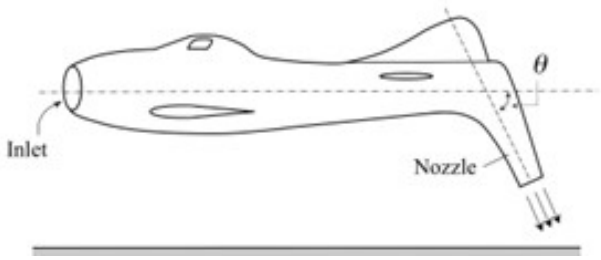

Figure 6.2: Jet Aircraft Before

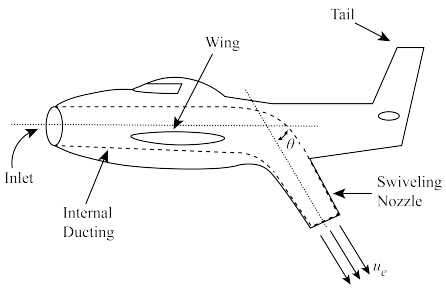

Figure 6.3: Jet Aircraft After

In the third example below, Figure 6.4 and Figure 6.5 show how the scaling of a Borda mouthpiece question was adjusted to convey a more realistic depiction. The length of the exit channel for the Borda mouthpiece was extended, consistent with the question statement regarding the mixing process taking roughly five duct heights to complete [14]. The extended exit channel is more representative of the actual scenario.

Question

We assumed that the exit jet from the Borda mouthpiece in problem 4 [refers to previous question] exited without mixing. If the exit duct is long enough, however, say greater than five duct heights, the jet can fully mix with the still fluid, so the exit flow fills the duct, as sketched below .

(a) Is there any change in the flow rate through the exit duct? If so, why?

(b) Is there any change in the force on the chamber?

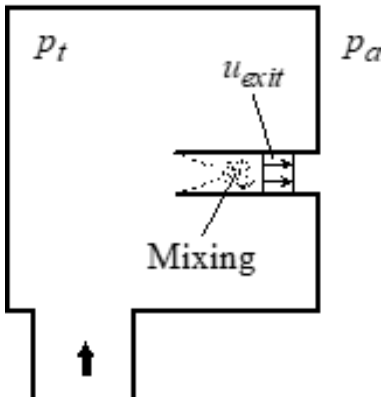

Figure 6.4: Borda Mouthpiece Before

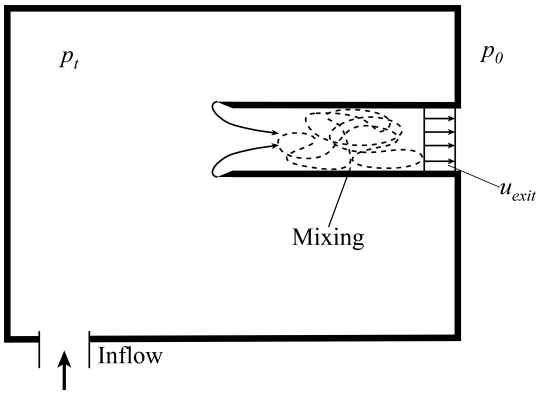

Figure 6.5: Borda Mouthpiece After

Image Creation for a Question

The question below did not originally have a figure associated with it. The addition of Figure 6.6 was done to avoid misinterpretation of the question and to keep the reader focused on the important aspects of the problem, which are the engine fan face, and the venturi nozzles. Moreover, it provides a visual reference for the reader who may not have seen an indoor test cell before.

Question

A gas turbine aeroengine is operated in an indoor test cell. The physical mass flow into the engine at standard day static conditions is 700 kg/s and the engine fan face Mach number is 0.5. The flow is measured using upstream choked converging-diverging nozzles ('Venturis'). Atmospheric air is drawn in through these nozzles, which discharge into a large chamber upstream of the engine. The nozzles are designed so shock losses are small, and we assume the combination of shock and viscous losses in the nozzles, plus the mixing losses in the process of discharge into the chamber, to be such that the ratio of stagnation pressure in the

chamber, p_{t_c}, to atmospheric pressure, p_{t_a}, is $p_{t_c}/p_{t_a} = 0.9$. A sketch of the test cell is given below.

(a) What is the engine fan face area? (What engine diameter might this imply?)

(b) What is the combined (i.e., total) throat area of the measurement nozzles?

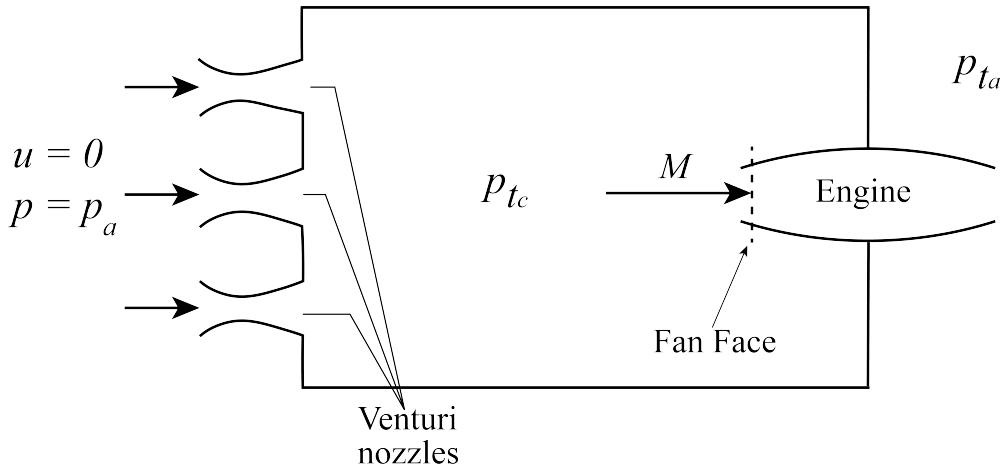

Figure 6.6: The figure generated for the Concept Question is a simplified diagram representing an aeroengine test cell.

Answering Questions

The following two examples are questions that required answers. The first question had a partial answer, which was edited and appended. The second required generation of an answer from scratch.

Question

For a two-stream compound-compressible flow through a converging-diverging nozzle:

(a) If the flow passes through a choked throat, and one of the two streams has $M = 1$ at the throat, what is the Mach number of the other stream?

(b) If the stagnation temperature of one stream were doubled, how would the Mach number at the throat change in that stream?

(c) If the stagnation temperature of one stream were doubled, how would the physical mass flow change in that stream?

Initial Answer

The behavior depends on whether the flow is compound choked or not. Compound choking is indicated by the sign of the compound flow indicator, β, [14]

$$\beta = \frac{A_1}{\gamma_1}(\frac{1}{M_1^2} - 1) + \frac{A_2}{\gamma_2}(\frac{1}{M_2^2} - 1). \tag{6.1}$$

Considered that the throat of the nozzle is choked, the value of β is less than zero so the flow is compound-choked and the mass flow will not change when the back pressure is dropped

Updated Answer

(a) *For a compound-compressible flow to be choked, the compound flow indicator,β, must be zero. From the definition of β:*

$$\beta = \frac{A_1}{\gamma_1}(\frac{1}{M_1^2} - 1) + \frac{A_2}{\gamma_2}(\frac{1}{M_2^2} - 1). \tag{6.2}$$

If the flow in one stream has $M = 1$ at the throat, the other stream must also have $M = 1$. The static pressure is uniform across the two streams, and the stagnation pressure in the two streams is also the same.

(b) *Changing the stagnation temperature of either stream has no effect on the Mach numbers or the static pressure field. The Mach numbers stay the same. This is an example of the Munk and Prim substitution principle[3] : for a steady, inviscid, adiabatic flow, the flow pattern and Mach number distribution do not depend on stagnation temperature. A given set of streamlines has the same pressure distribution independent of stagnation temperature, and thus keeps the flow in equilibrium if the quantity u^2/T, or equivalently stream Mach number, is unchanged. The velocity is proportional to the square root of stagnation temperature to keep the same Mach number.*

(c) *The corrected flow per unit area remains the same independent of the stagnation temperature, so the temperature-corrected mass flow per unit area, $\dot{m}/\sqrt{T_t}$ remains the same. The physical mass flow in a stream is thus proportional to $1/\sqrt{T_t}$.*

Question

Consider the frictionless flow through a turbomachinery stage made up of a row of stationary blades followed by a row of moving blades. A view of the stage is given in the figure on the left, which shows a constant radius, constant height duct with the stage blade rows. The figure on the right shows a radial view of the two blade rows. The flow upstream of the stage is axial, i.e., there is no circumferential velocity component, and subsonic. As seen in the stationary reference frame the first row turns the flow from axial at station 1 to 60 degrees from axial at station 2. The second row returns the flow to axial, as seen in the stationary reference frame, at station 3. In the relative frame, the flow from the inlet to the second row

[3]See chapters 10 and 11 from Internal Flow [14]

is axial. For questions (a) to (c) below, the flow is adiabatic, for (d) there is frictionless heat addition.

(a) What direction is the rotor moving in the configuration in Figure 2b?

(b) If the area of the blade channel in the first row is a minimum at the blade channel exit, what can you say about the Mach number there?

(c) Sketch the velocity vector triangle between the exit velocity from the stator, as seen in the stationary system, and the inlet relative velocity into the rotor (the velocity in the rotor fixed reference frame).

(d) Suppose the stator is choked, with T_t, the stagnation temperature upstream of the stage. A small amount of heat, dq, per unit mass is planned to be added upstream of the stage, but it is desired to keep the physical mass flow (kg/s) through the turbine, and the stator exit Mach number, the same as without the heat addition. Is the heat addition feasible?

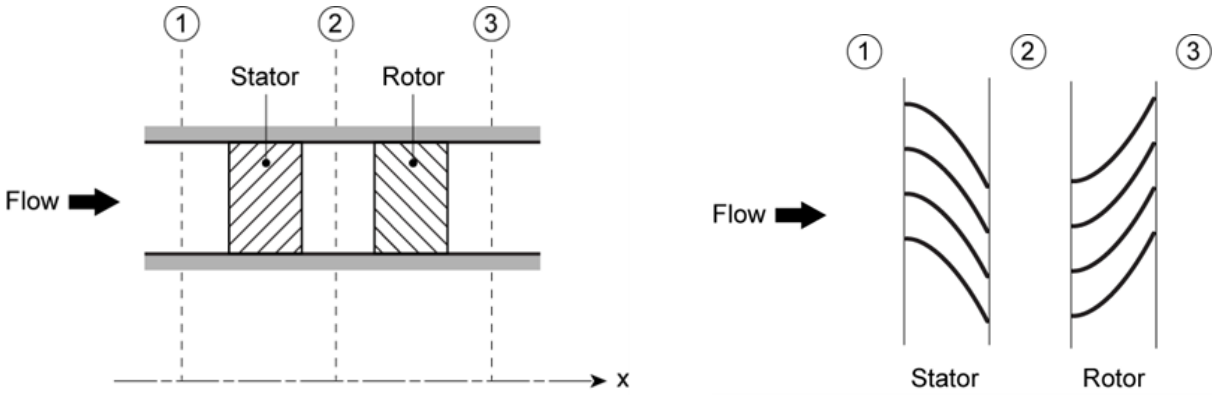

Figure 6.7: A turbomachinery stage. Figure (a) is a side view, Figure (b) is a view looking radially inwards.

Generated Answer

(a) The rotor will move downwards. This ensures that the flow exiting at station 3 can be axial. The flow exits the stator 60 degrees from axial, to turn the flow back to axial, a force must be applied to the fluid opposite to the direction of the fluid motion.

(b) If the area of the blade channel is in the first row is a minimum at the blade channel exit, this indicates a narrowing in the blade row passage, similar to a converging duct. From 1D flow arguments, a decrease in area for subsonic flow results in an increase in Mach number. The Mach number at the blade channel exit will thus be at a maximum.

(c) The velocity triangles are shown below.

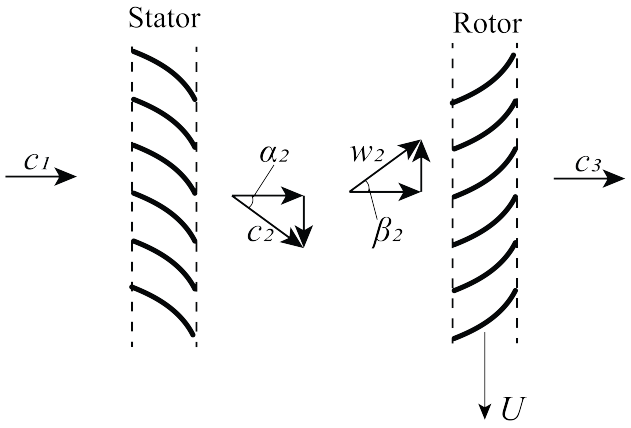

Figure 6.8: Velocity triangles for the rotor and stator resulting in axial exit flow.

(d) If heat is added upstream of the stage, the stagnation temperature upstream of the stage T_t will increase ($dq = c_p dT_t$) and the stagnation pressure will decrease. If the flow is choked, this leads to the upstream physical mass flow rate decreasing. To keep both the physical mass flow through the turbine and the stator exit Mach number constant, the upstream stagnation pressure must increase to keep the correct flow constant.

6.3 Summary of Concept Question Work

The (proposed) titles of chapters for which questions have been edited are:

1. Introductory Flow Concepts
2. Control Volume Analysis
3. Compressible Channel Flow
4. Static and Stagnation Pressure Fields
5. Vorticity and Circulation
6. Flow in Rotating Passages
7. Thermo-fluid Processes and Loss

At the time of this thesis submission, I have restructured and edited over 250 Concept Questions and answers. The advice presented here on creation of concept questions stems from my learnings throughout this process. In addition to this work, I have also edited chapter

prefaces which present the basic concepts for each chapter. I took a course in Internal Flows (16.120) at MIT with Dr. Greitzer, and through my work on this book, I have approached the material from the position of both student and author, requiring immersion in, and full comprehension of, the range of topics within this book. The discussions concerning the Concept Questions have enhanced my ability to communicate complex concepts, and my knowledge of fluids has been widened and deepened.

Appendix A

A.1 Analysis of Rotating Stall Inception Using Spatial Fourier Coefficients (SFC)

The growth rate of the flow perturbations has been reported for the computed spatial Fourier coefficients of the pressure perturbations at the disk face. A linear fit of the SFC magnitude for the *first* harmonic, is shown in Figure A.1. The fit is taken based on the data for perturbation magnitudes of 10^{-3} to 10^{-2}, such that the perturbations are small relative to the mean flow.

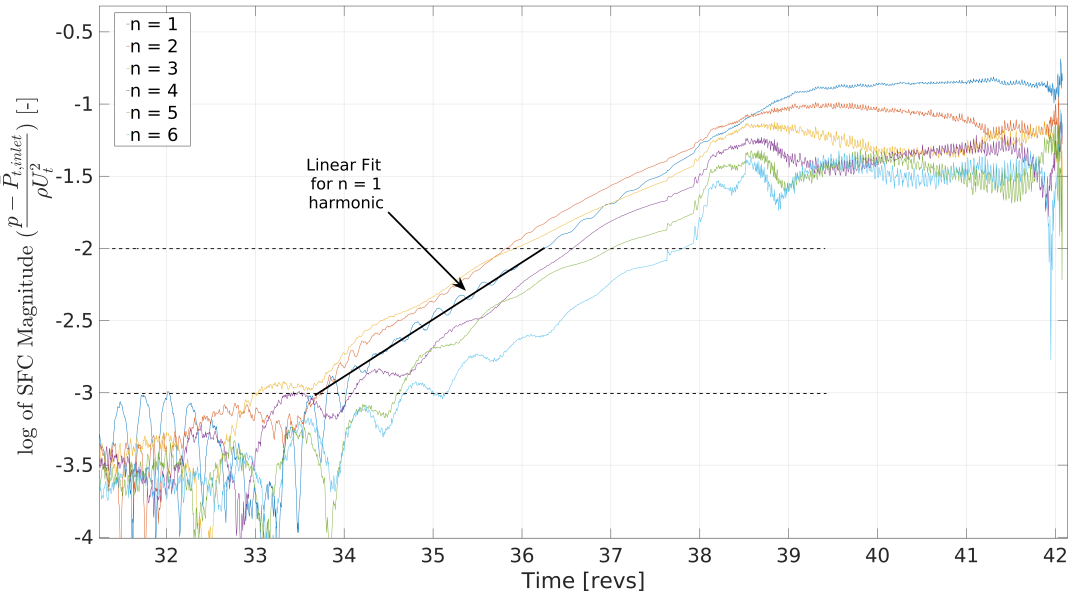

Figure A.1: Spatial Fourier Coefficients for harmonics 1 through 6 for $d\psi/d\phi = 0.30$ case.

A.1.1 Comparison of Growth Rate of Pressure and Velocity Perturbations

The pressure and velocity perturbations, $\frac{P-\bar{P}}{\rho\bar{U}^2}$ and $\frac{\delta V_x}{\bar{U}}$, are of the same magnitude compared to the mean flow. The growth rates for both pressure and velocity are eigenvalues of the system and should be the same - the numerical results show that they are in good agreement and either one can be used to define rotating stall inception.

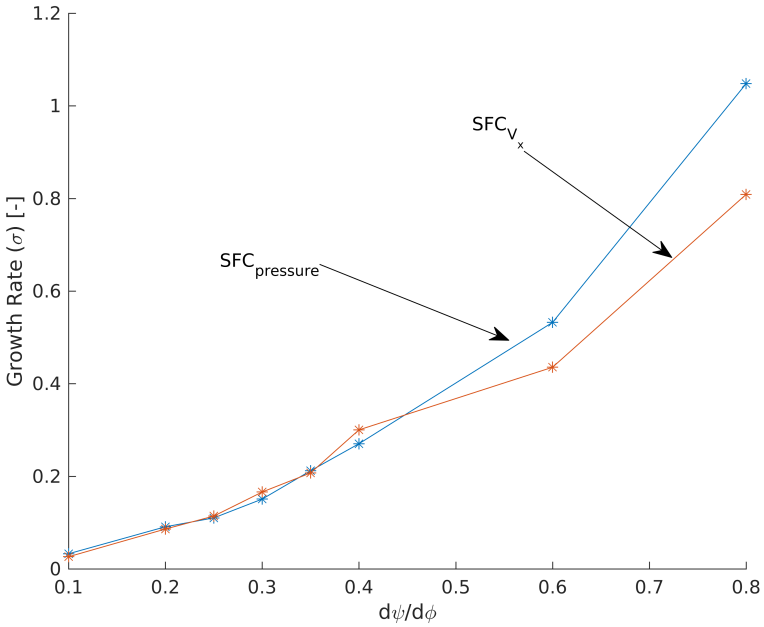

Figure A.2: Growth rate of perturbations (first harmonic) calculated using 1) SFC of the non-dimensional pressure perturbations, and 2) SFC of the non-dimensional axial velocity perturbations.

A.2 Spatial Fourier Decomposition for $d\psi/d\phi = 0.6$

To explain the difference in SFC size between harmonics for mode-like versus spike-like stall inception, higher harmonics (past the n=6) plotted in Figure 4.4 were considered. The SFC magnitude for a given harmonic is dependent on the amplitude and waveform of a signal. Modal stall inception is smooth and sinusoidal at the beginning of the stall inception regime, thus the SFCs of lower order harmonics will be greater in magnitude compared to those of higher harmonics. To resolve greater amplitude, spike-like pressure traces, the coefficients of higher harmonics will be similar in magnitude to those of lower harmonics (from the beginning of the stall inception regime). By this reasoning, for steeper characteristic slopes, if a large number of harmonics are plotted, there will be an eventual decay in magnitude of the SFCs of higher harmonics relative to lower ones. This is shown in Figure A.3 for a characteristic slope $d\psi/d\phi = 0.6$. The black dashed lines indicate the stall inception regime.

The coefficients of the fifteen and sixteenth harmonics reach 10^{-3} over half a rotor revolution after the first four harmonics as they were nearly an order of magnitude smaller in size at the beginning of the stall inception regime.

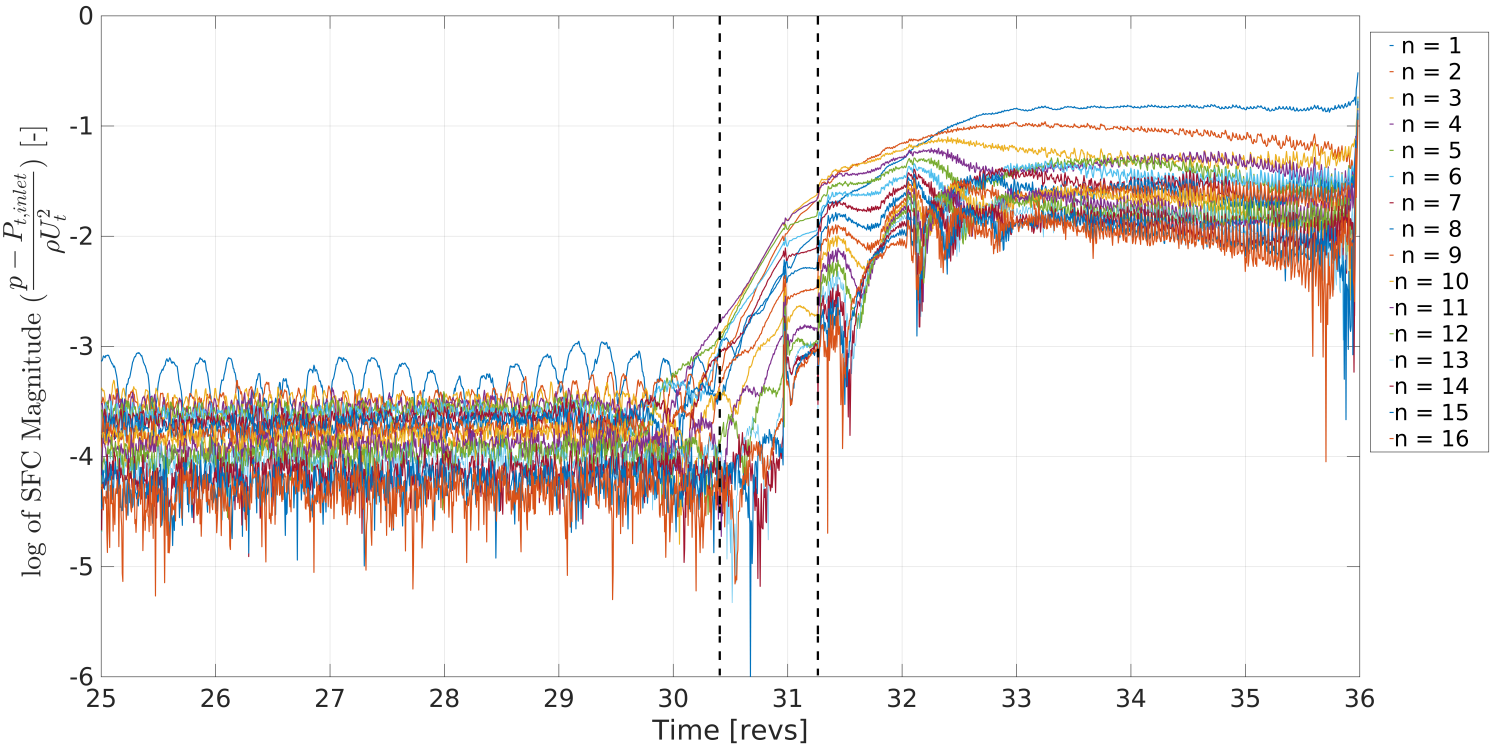

Figure A.3: Rotating stall SFC's for $d\psi/d\phi = 0.60$, first 16 harmonics.

A.3 Spatial Fourier Decomposition for $d\psi/d\phi = 0.2$

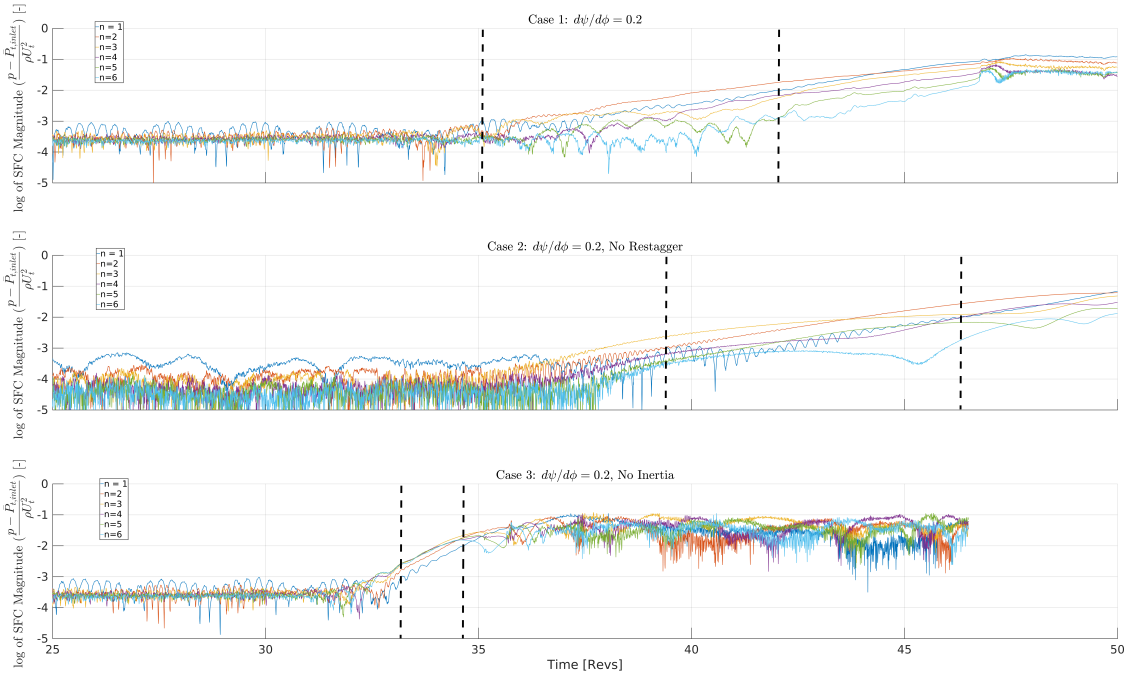

Figure A.4: SFC for $d\psi/d\phi = 0.2$ 1) Case with restagger and inertia 2) Case with inertia, but without restagger 3) Case with restagger, but without inertia. The black dashed lines indicate the rotating stall inception regime.

Appendix B

B.1 Comparison of Compressor Pressure Rise Characteristics

To clarify the difference between the simulations performed in this thesis and those done by Logrono, the growth rates as a function of characteristic slope are compared in Figure B.1. Logrono used a linear, positively sloped characteristic for unsteady calculations, with a blade restagger of 0.01 RMS (averaged for all circumferential points around the actuator disk). The same blade exit angle, 51.45°, and inertial parameter, $\lambda_{rotor} = 0.2$, were used as in the present work [8]. The simulations done by Logrono are in better agreement with theory for a characteristic slope, $d\psi/d\phi < 0.2$, however they begin to diverge faster from theory for steeper sloped cases, and the solver fails sooner, for slopes, $d\psi/d\phi \geq 0.4$, as shown in [8]. This thesis thus used the cubic plus linear characteristic to enable investigation of steeper characteristic slopes.

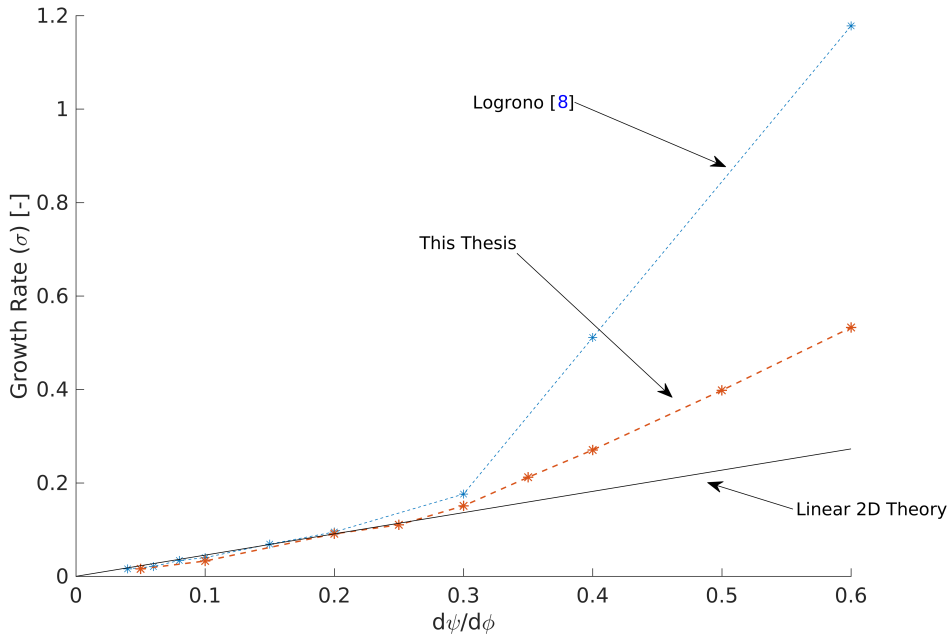

Figure B.1: Comparison of growth rates calculated by Logrono to those done in this thesis, and to 2D theory.

Appendix C

C.1 The Role of Asymmetric Rotor Restagger in TBLOCK Modeling of Rotating Stall

To show that blade restagger, or another form of asymmetry, is needed to simulate rotating stall in TBLOCK for steeper sloped cases, the pressure traces for a slope of $d\psi/d\phi = 0.6$ are compared for a case with blade restagger to one without it, Figure C.1. The red dashed line denotes the beginning of the stall inception regime. For no restagger, the blue circle shows the variations in the pressure traces that are not a part of the spike formation.

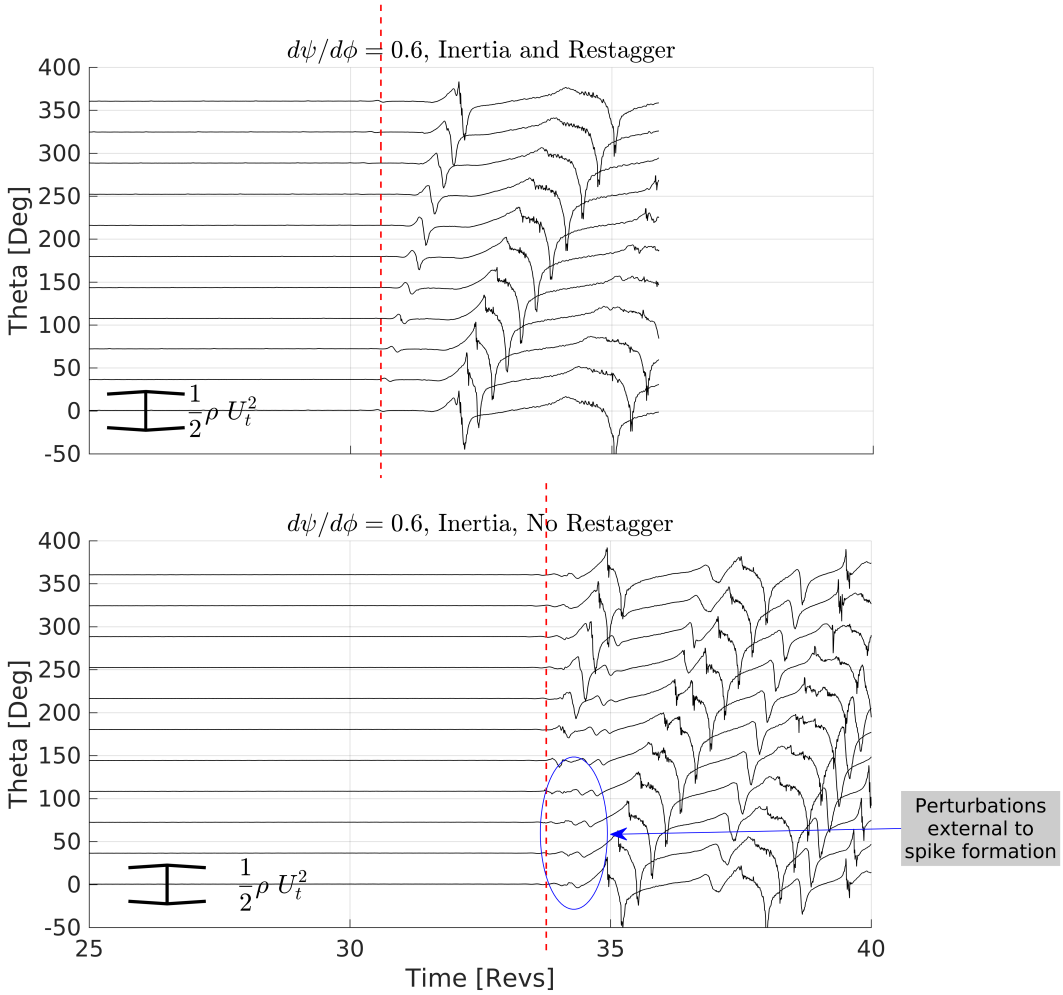

Figure C.1: Pressure perturbations for $d\psi/d\phi = 0.6$ with and without blade restagger.

The requirement of asymmetry to simulate stall cell formation in TBLOCK is further exemplified by plots of the variation in flow coefficient, ϕ, around the rotor diskface for $d\psi/d\phi = 0.8$. Figure C.2 shows the stall cell formation as a function of time with blade restagger, and Figure C.3 shows the formation without blade restagger. Both figures are designed to give a view of an annulus region corresponding to a HTR = 0.75 to indicate how perturbations would rotate around the annulus. In Figure C.2, a circumferential section of the rotor annulus develops into a region of flow with a reduced ϕ, rotating around the annulus at a rate less than the rotor frequency Ω. This full span stall develops within two rotor revolutions. Without restagger, Figure C.3, the flow stalls in less than one rotor revolution, and there appears to be two stalled regions that span a small radial section of the annulus.

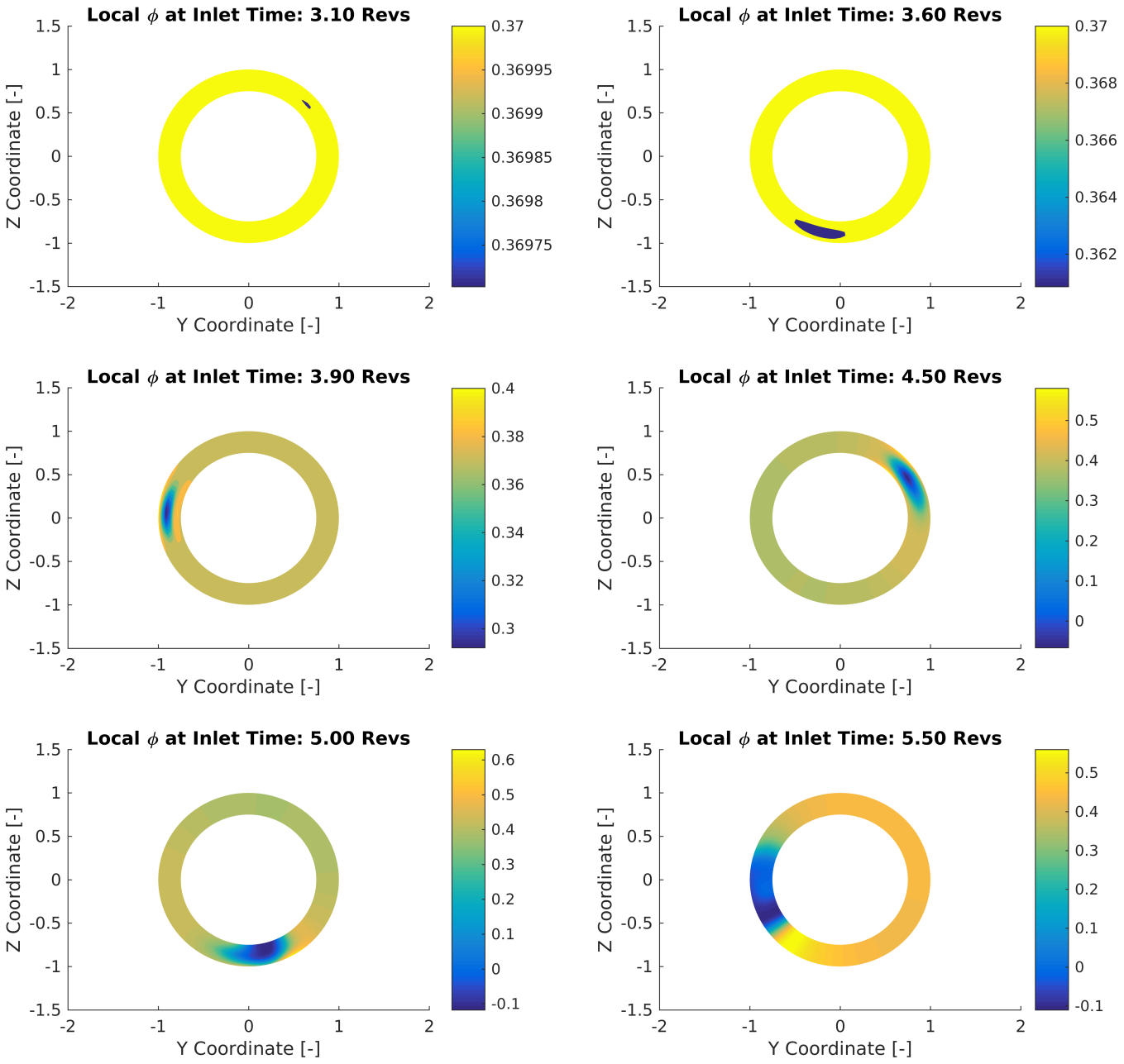

Figure C.2: $d\psi/d\phi = 0.8$ case with blade passage inertia and blade restagger. Annulus view of the wedge geometry. The stall cell rotates clockwise, in the direction of rotor rotation.

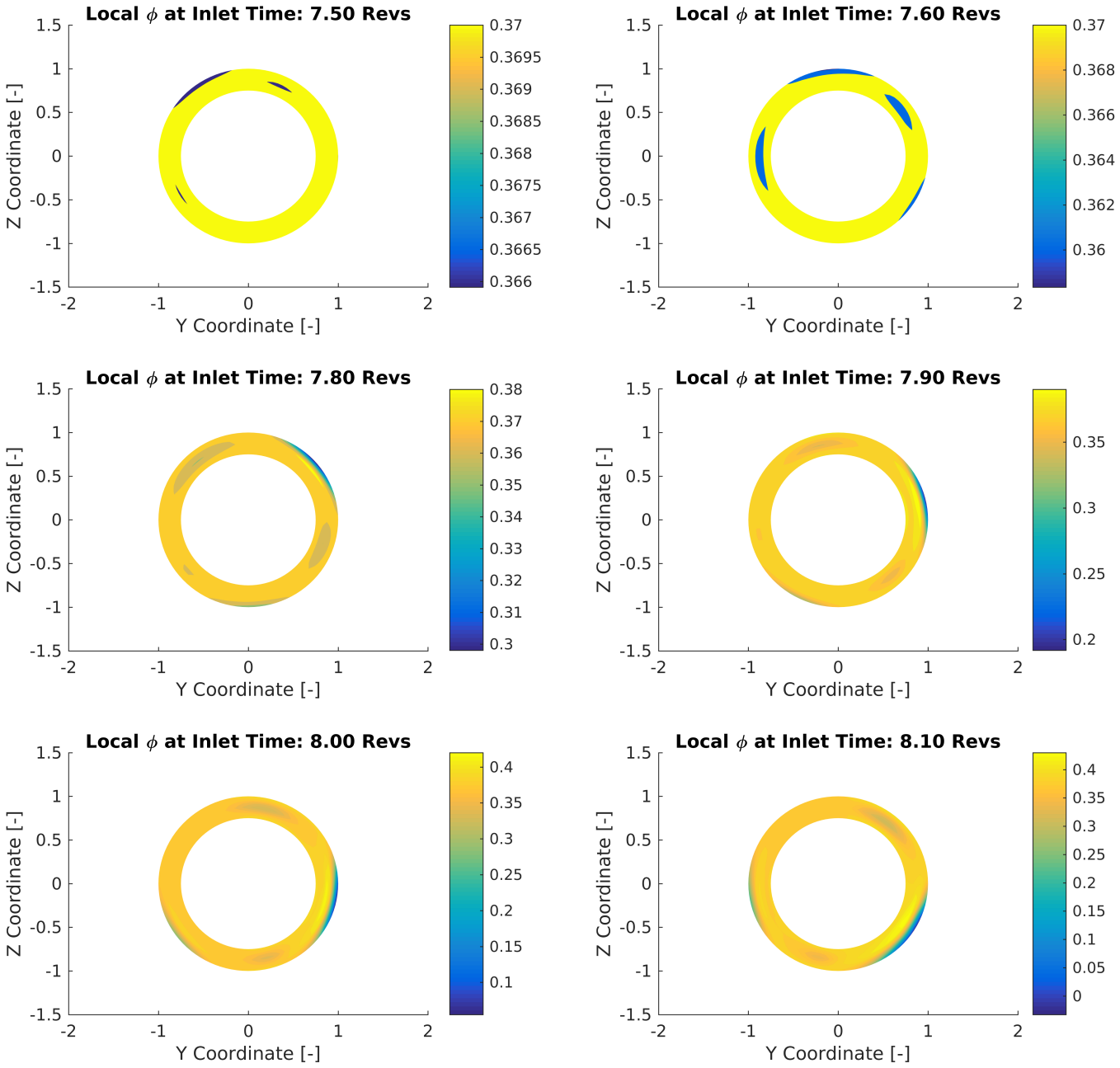

Figure C.3: $d\psi/d\phi = 0.8$ case with blade passage inertia, but no blade restagger. Annulus view of the wedge geometry. The stalled region rotates clockwise, in the direction of rotor rotation.

Appendix D

D.1 Ratio of Radial to Axial Velocity Perturbations During Rotating Stall Inception

For slopes greater than 0.35, the ratio of the radial perturbations relative to the axial perturbations, $\frac{RMS(\delta V_r)}{RMS(\delta V_x)}$, Figure D.1 and Figure D.2, increases within the stall inception regime (pressure perturbations between 10^{-3} and 10^{-2} of the mean dynamic pressure). This suggests that radial perturbations cannot be neglected during stall inception for $d\psi/d\phi \geq 0.35$. The black dashed lines denote the time interval of the stall inception regime (the magnitude of the first harmonic of the pressure perturbations is between 10^{-3} and 10^{-2}). Figure D.2 shows the transition to three dimensional flow.

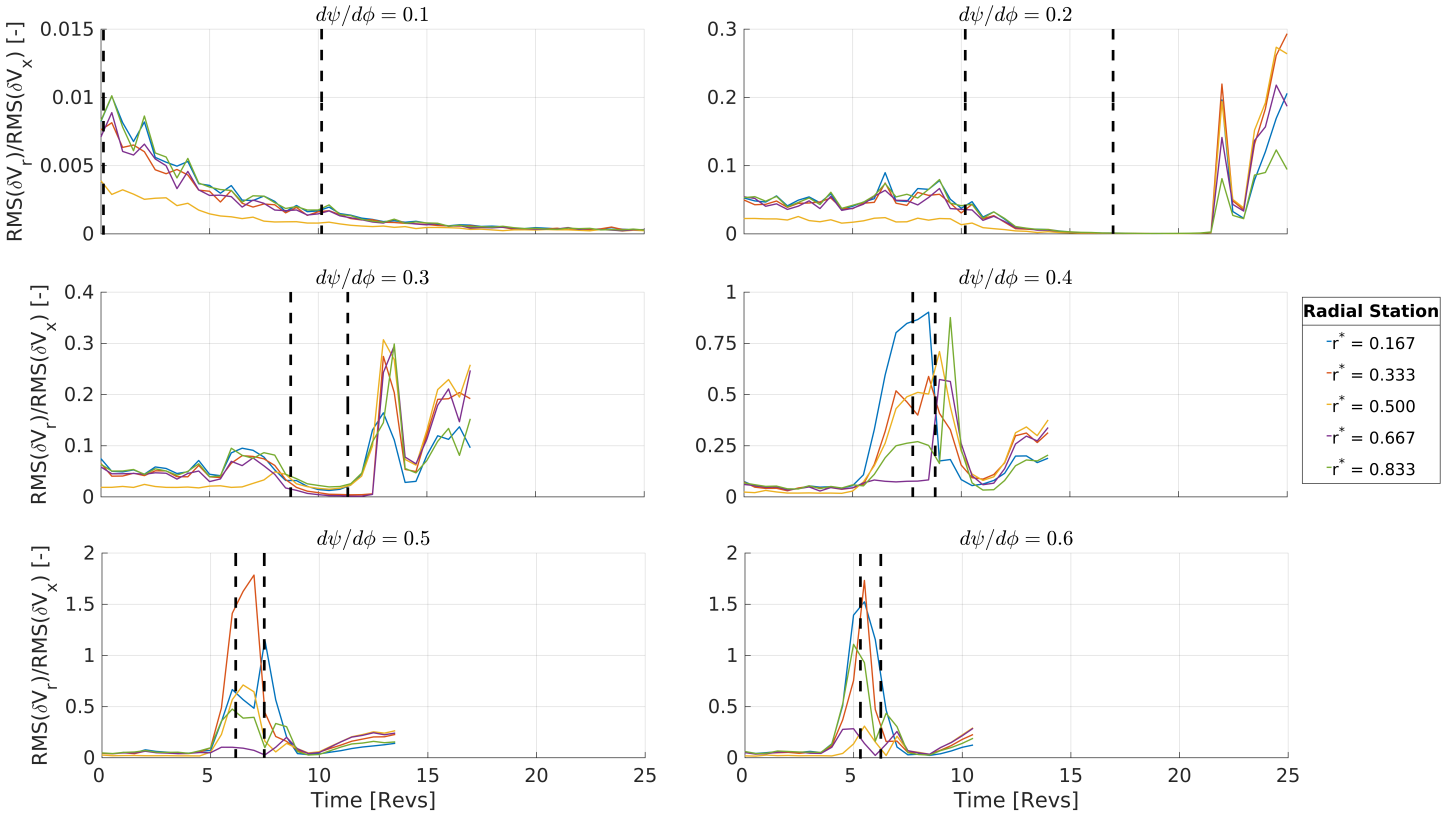

Figure D.1: Ratio of the RMS radial to axial velocity perturbations for $d\psi/d\phi = 0.10$ to 0.60 with blade restagger and blade passage inertia. The values at the five following radial stations are plotted: $r^* = 0.833$ green, $r^* = 0.667$ purple, $r^* = 0.500$ yellow, $r^* = 0.333$ orange, $r^* = 0.167$ blue.

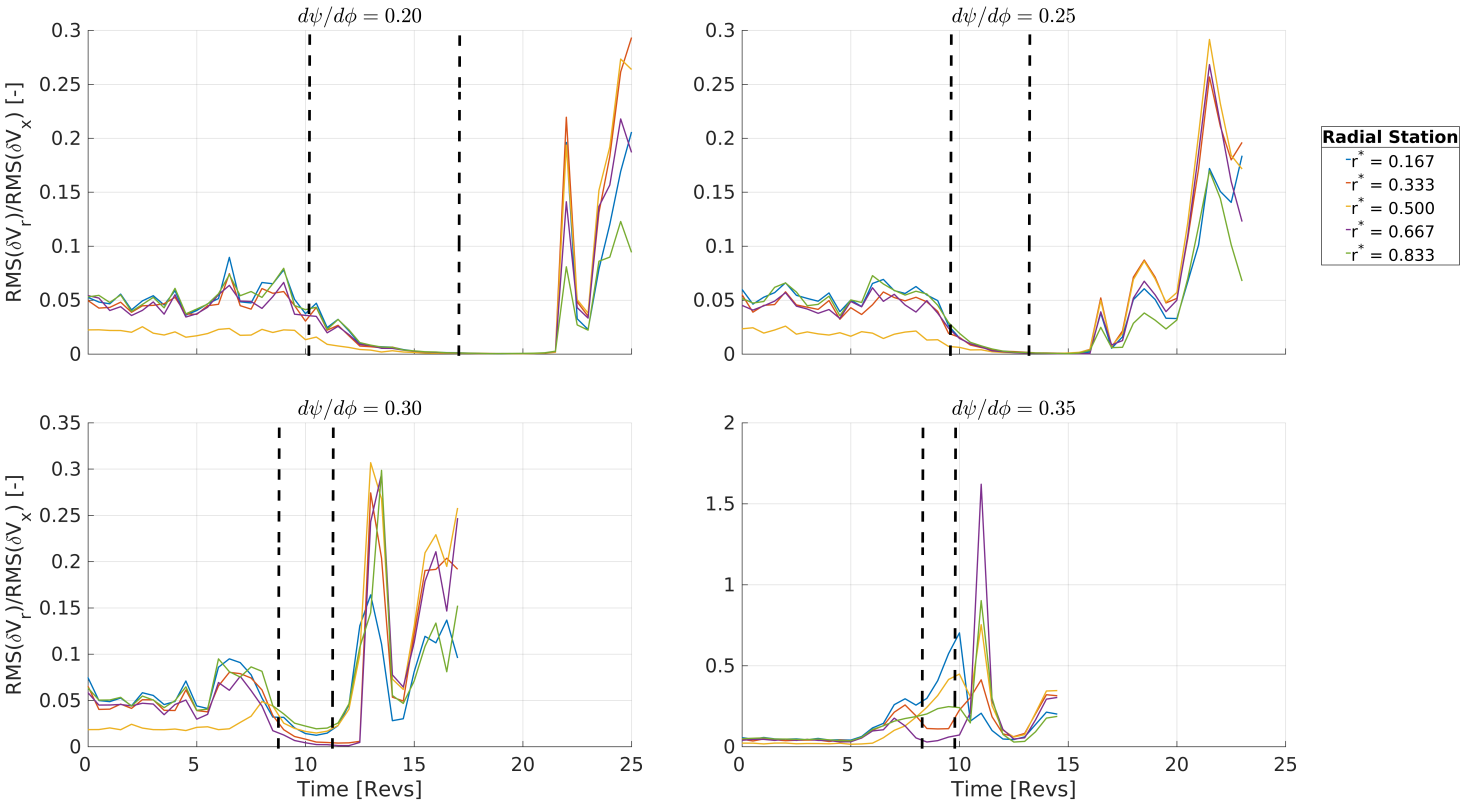

Figure D.2: Ratio of RMS radial to axial velocity perturbations for $d\psi/d\phi = 0.20$ to 0.35 with blade restagger and blade passage inertia. The values at the five following radial stations are plotted: $r^* = 0.833$ green, $r^* = 0.667$ purple, $r^* = 0.500$ yellow, $r^* = 0.333$ orange, $r^* = 0.167$ blue.

Characteristic Slope $d\psi/d\phi = 0.2$ Without Blade Passage Inertia and Blade Restagger

To further exemplify the ineffectiveness of blade passage inertia and blade restagger on departure of stall inception from two-dimensionality, Figure D.3 shows $\frac{RMS(\delta V_r)}{RMS(\delta V_x)}$, where the black dashed lines denotes the stall inception regime. Arrows indicate the value of $\frac{RMS(\delta V_r)}{RMS(\delta V_x)}$ at the first observation of rotating stall[1] (A comparison of the SFC plots is given in Figure A.4). During stall inception, there is a decrease in relative velocity magnitude of radial perturbations for all three cases, with the radial velocity perturbations an order of magnitude lower than the axial perturbations. The value of $\frac{RMS(\delta V_r)}{RMS(\delta V_x)} \leq 0.041$ for the entirety of the stall inception regime for each case, indicating that blade passage inertia and blade restagger do not have an effect on the dimensionality of stall. The behavior of the perturbations outside of the stall inception regime will not be discussed here, but should be looked at in future work.

[1] defined in Section 2.1.1

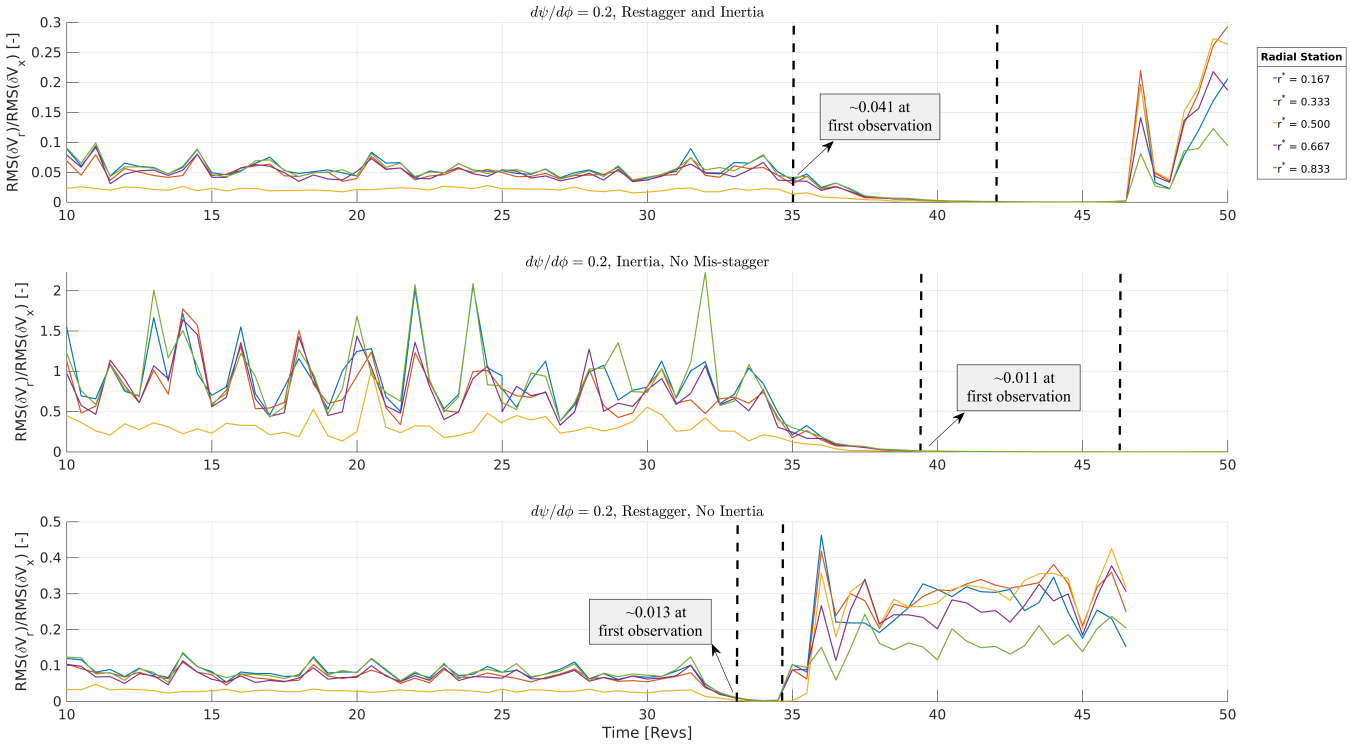

Figure D.3: $d\psi/d\phi = 0.2$ showing the ratio of the radial to axial RMS velocity perturbations for each case from top to bottom: 1) Case with blade restagger and blade passage inertia 2) Case with inertia, but without restagger 3) Case with restagger, but without inertia. The values at the five following radial stations are plotted: $r^* = 0.833$ green, $r^* = 0.667$ purple, $r^* = 0.500$ yellow, $r^* = 0.333$ orange, $r^* = 0.167$ blue.

References

[1] N. A. Cumpsty, "Compressor aerodynamics," in Krieger Publishing Company, 2004, ch. 9, Stall and Surge.

[2] I. J. Day, "Stall inception in axial flow compressors," *Journal of Turbomachinery*, vol. 115, pp. 1–9, 1993. DOI: 10.1115/1.2929209.

[3] A. H. Stenning, "Rotating stall and surge," *ASME Journal of Fluids Engineering*, vol. 102, no. 1, pp. 14–20, 1980. DOI: 10.1115/1.3240618.

[4] J. P. Longley, "A review of nonsteady flow models for compressor stability," *ASME Journal of Turbomachinery*, vol. 116, no. 2, pp. 202–215, 1994. DOI: 10.1115/1.2928354.

[5] T. R. Camp and I. J. Day, "A study of spike and modal stall phenomena in a low-speed axial compressor," *ASME Journal of Turbomachinery*, vol. 120, no. 3, pp. 393–401, 1998. DOI: 10.1115/1.2841730.

[6] G. Pullan, A. M. Young, I. J. Day, E. M. Greitzer, and Z. S. Spakovszky, "Origins and structure of spike-type rotating stall," *ASME Journal of Turbomachinery*, vol. 137, no. 5, 2015. DOI: 10.1115/1.4028494.

[7] F. K. Moore and E. M. Greitzer, "Theory of post-stall transients in axialcompression systems: Part i — development of equations," *ASME Journal of Engineering for Gas Turbines and Power*, vol. 108, no. 1, pp. 68–76, 1986. DOI: 10.1115/1.3239887.

[8] M. Logrono, "A unified framework for characterization of mode and spike routes to rotating stall," M.S. thesis, Department of Aeronautics and Astronautics, Massachusetts Institute of Technology, 2024.

[9] G. Pullan, E. M. Greitzer, Z. S. Spakovszky, and S. D. Grimshaw, *A unified framework for compressor stall inception*, Internal Presentation, MHI Turbomachinery Workshop, Takasago, Japan, Apr. 2023.

[10] Z. S. Spakovszky, "Applications of axial and radial compressor dynamic system modeling," Ph.D. dissertation, Massachusetts Institute of Technology, Cambridge, MA, 2001.

[11] W. G. Joo and T. P. Hynes, "The simulation of turbomachinery blade rows in asymmetric flow using actuator disks," *ASME Journal of Turbomachinery*, vol. 119, no. 4, pp. 723–732, 1997. DOI: 10.1115/1.2841182.

[12] F. K. Moore, "Theory of rotating stall of multistage axial compressors: Part i —small disturbances," *ASME Journal of Engineering for Gas Turbines and Power*, vol. 106, no. 2, pp. 313–320, 1984. DOI: 10.1115/1.3239565.

[13] G. Pullan, *Personal communication*, July 25, 2024.

[14] E. M. Greitzer, C. S. Tan, and M. B. Graf, *Internal Flow: Concepts and Applications*. Cambridge University Press, 2004.

[15] G. Tovstiga, "Strategy praxis. management for professionals," in Springer, 2023, ch. What Is First Principles Thinking? ISBN: 978-3-031-40692-8.